

AD-756 937

INTERFEROMETRIC AND PHOTOMETRIC  
STUDIES OF BARIUM RELEASES. PART A

M. A. Biondi, et al

Pittsburgh University

Prepared for:

Advanced Research Projects Agency

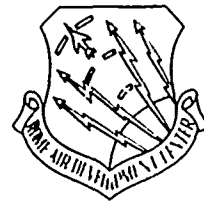
August 1971

DISTRIBUTED BY:

**NTIS**

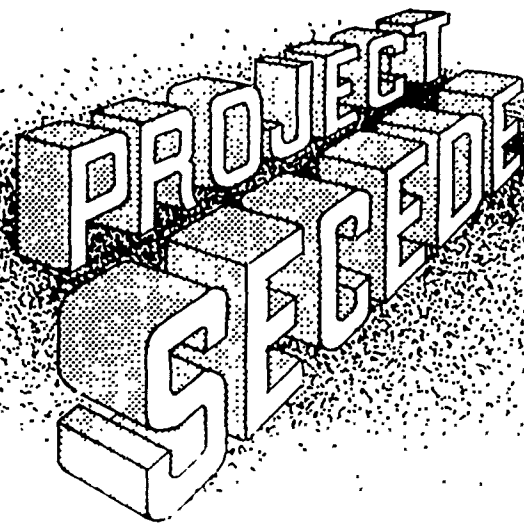
National Technical Information Service  
U. S. DEPARTMENT OF COMMERCE  
5285 Port Royal Road, Springfield Va. 22151

RADC-TR-71-222, PART A  
FINAL TECHNICAL REPORT  
AUGUST 1971



PREPARED BY  
RADC AIR DEVELOPMENT CENTER  
AIR FORCE SYSTEMS COMMAND  
GRIFFISS AIR FORCE BASE, NEW YORK 13440

AD 756937



# INTERFEROMETRIC AND PHOTOMETRIC STUDIES OF BARIUM RELEASES

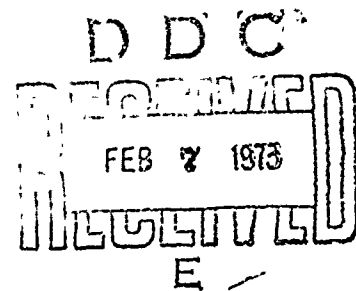
PART A

UNIVERSITY OF PITTSBURGH

SPONSORED BY  
ADVANCED RESEARCH PROJECTS AGENCY  
ARPA ORDER NO. 1057

Reproduced by  
NATIONAL TECHNICAL  
INFORMATION SERVICE  
U S Department of Commerce  
Springfield VA 22151

APPROVED FOR PUBLIC RELEASE;  
DISTRIBUTION UNLIMITED.



THE VIEWS AND CONCLUSIONS CONTAINED IN THIS DOCUMENT ARE THOSE OF THE  
AUTHORS AND SHOULD NOT BE INTERPRETED AS NECESSARILY REPRESENTING THE  
OFFICIAL POLICIES, EITHER EXPRESSED OR IMPLIED, OF THE ADVANCED RESEARCH  
PROJECTS AGENCY OR THE U. S. GOVERNMENT.

7-222-1 17-73500

When US Government drawings, specifications, or other data are used for any purpose other than a definitely related government procurement operation, the government thereby incurs no responsibility nor any obligation whatsoever; and the fact that the government may have formulated, furnished, or in any way supplied the said drawings, specifications, or other data is not to be regarded, by implication or otherwise, as in any manner licensing the holder or any other person or corporation, or conveying any rights or permission to manufacture, use, or sell any patented invention that may in any way be related thereto.

AVAILABILITY CODES		
DATE		
A		

UNCLASSIFIED

Security Classification

DOCUMENT CONTROL DATA - R & D		
<i>(Security classification of title, body of abstract and indexing annotation must be entered when the overall report is classified)</i>		
1. ORIGINATING ACTIVITY (Corporate author) University of Pittsburgh 3117A Cathedral of Learning Pittsburgh, PA 15213		2a. REPORT SECURITY CLASSIFICATION UNCLASSIFIED
3. REPORT TITLE Interferometric and Photometric Studies of Barium Releases		2b. GROUP
4. DESCRIPTIVE NOTES (Type of report and inclusive dates) FINAL REPORT "A" 27 Oct 69 to 30 Jun 71		
5. AUTHOR(S) (First name, middle initial, last name) M.A. Biondi R.D. Hake, Jr. D.P. Sipler		
6. REPORT DATE August 1971	7a. TOTAL NO OF PAGES 74	7b. NO OF REFS 16
8a. CONTRACT OR GRANT NO. F30602-70-C-0099	9a. ORIGINATOR'S REPORT NUMBER(S)	
b. PROJECT NO. ARPA Order 1057	9b. OTHER REPORT NO(S) (Any other numbers that may be assigned this report)	
c. Program Code OE20	RADC-TR-71-222, Part A	
d.		
10. DISTRIBUTION STATEMENT Approved for public release; distribution unlimited.		
11. SUPPLEMENTARY NOTES Monitored by: Richard A. Schneible RADC/OCSE Griffiss AFB NY 13440	12. SPONSORING MILITARY ACTIVITY Advanced Research Projects Agency 1400 Wilson Blvd Arlington VA 22209	
13. ABSTRACT Two distinct tasks are covered by this final report; (1) reduction of optical interferometer data obtained during the 1969 SECEDE III barium release observations in Alaska, and (2) optical interferometer instrumentation, observations, and preliminary data reduction for the 1971 SECEDE II barium release series in Florida. Analysis of the SECEDE III data shows that, even at late times, optical surface brightness of the barium ion clouds (as obtained from filter photography) can not be transformed in ion column densities without applying a spatially varying correction factor, owing to substantial resonance absorption of the incoming sunlight as it penetrates the cloud. To avoid resonance absorption effects a larger (4 inch aperture) interferometer coupled to a 16" telescope was constructed for the 1971 SECEDE II series in Florida. This interferometer was operated in a wavelength scanning mode and in a spatial scanning mode (locked on a weakly absorbed line frequency to minimize resonance absorption effects).		

DD FORM 1 NOV 62 1473

I

UNCLASSIFIED  
Security Classification

14 KEY WORDS	LINK A		LINK B		LINK C	
	ROLE	WT	ROLE	WT	ROLE	WT
Barium ion cloud Upper- atmosphere studies Optical Interferometer						

II

INTERFEROMETRIC AND PHOTOMETRIC STUDIES OF BARIUM RELEASES  
Part A

M. A. Biondi  
R. D. Hake, Jr.  
D. P. Sipler

Contractor: University of Pittsburgh  
Contract Number: F30602-70-C-0099  
Effective Date of Contract: 29 October 1969  
Contract Expiration Date: 30 June 1971  
Amount of Contract: \$74,876.00  
Program Code Number: OE20

Principal Investigator: M. A. Biondi  
Phone: 412 621-3500

Project Engineer: Vincent J. Coyne  
Phone: 315 330-3107

Contract Engineer: Richard A. Schneible  
Phone: 315 330- 3451

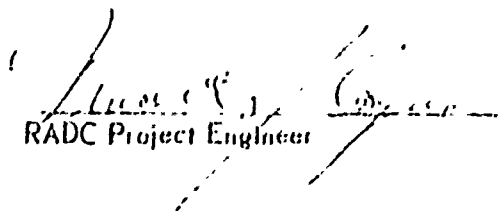
Approved for public release:  
distribution unlimited.

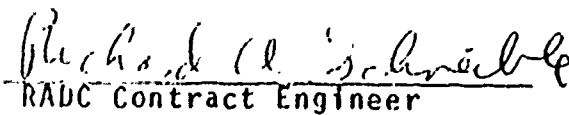
This research was supported by the  
Advanced Research Projects Agency  
of the Department of Defense and was  
monitored by Richard A. Schneible  
RADC (OCSE), GAFB, NY 13440 under  
contract F30602-70-C-0099.

III

PUBLICATION REVIEW

This technical report has been reviewed and is approved.

  
RADC Project Engineer

  
RADC Contract Engineer

IV

FINAL REPORT A

"Interferometric and Photometric Studies of Barium Releases"

by

M. A. Biondi, R. D. Hake, Jr. and D. P. Sipler

Contract No. F30602-70-C-0099

Rome Air Development Center

Griffiss Air Force Base

New York 13440

27 October 1969 to 30 June 1971

Sponsored By  
Advanced Research Projects Agency  
ARPA Order No. 1057,  
Amd. #15

Principal Investigator: M. A. Biondi

Phone: (412)-621-3500

Project Engineer: Richard A. Schneible

Phone: (315)-330-3451

V



Technical Report Summary

Two distinct tasks are covered by this final report; (1) reduction of optical interferometer data obtained during 1969 Secede III barium release observations in Alaska, and (2) optical interferometer instrumentation, observations, and preliminary data reduction for the 1971 Secede II barium release series in Florida.

Optical interferometers of the Fabry-perot (F-P) type permit detailed measurements of the spectral line profiles resulting when sunlight is scattered from the neutral and ionized barium atoms released in the ionosphere as part of the Secede study series. From these measurements column densities and temperatures of the neutral and ionized barium can be deduced. Analysis of the voluminous data obtained with a medium sized (2 inch aperture) F-P interferometer observing the Alaskan Secede III releases was impeded by the fact that the data format was not suitable for computer reading, plotting and analysis. As one of the tasks of the contract, interfacing was constructed to transform the 1/4" magnetic tape records (containing data in pulse train and audio record form) to computer-compatible 1/2" magnetic tape in a word form readable by means of a computer program developed for the purpose. The records of the most important release, event GUM, were transcribed to 1/2" magnetic tape with this interfacing. Analysis of the Secede III data shows that, even at late times, optical surface brightness of the barium ion clouds (as obtained from filter photography) can not be transformed into ion column densities without applying a spatially varying correction factor, owing to substantial resonance absorption of the incoming sunlight as it penetrates the cloud. In addition, the interferometer data indicate that the neutral Ba atoms

remain quite hot ( $\sim 2000^\circ\text{K}$ ) for tens of seconds after release; thus thermal excitation of the barium to metastable levels may contribute significantly to the initial cloud ionization (supplementing the two-stage photo-ionization process usually invoked).

To avoid resonance absorption effects in transforming surface brightness of the ion cloud to ion column densities, a larger (4 inch aperture) interferometer coupled to a 16" telescope (to improve spatial resolution) was constructed for the 1971 Secede II series in Florida. The interferometer was operated in a wavelength scanning mode (to determine neutral and ionized barium atom temperatures) and in a spatial scanning mode (locked on a weakly absorbed line frequency) to minimize resonance absorption falsification of the ion column densities deduced from the ion cloud surface brightness. The time development of striations in the Secede II ion clouds was detected with the instrument and will be correlated with rf propagation experiments from a beacon passing behind the ion cloud (whose position is recorded on our videotape records obtained with a bore-sighted TV camera). The ion line profiles provide correction factors for filter photography of the cloud which permits relation of their measured surface brightnesses to the ion column densities at various positions in the cloud.

"Interferometric and Photometric Studies of Barium Releases"

M. A. Biondi, R. D. Hake, Jr. and D. P. Sipler  
University of Pittsburgh

This research was supported by the  
Advanced Research Projects Agency of  
The Department of Defense and was  
monitored by Rome Air Development Center,  
under Contract No. F30602-70-C-0099



---

M. A. Biondi  
Principal Investigator

## I. Introduction

This report summarizes our efforts in developing apparatus for optical observations of barium releases in the Secede series and for optical detection of ionospheric electron heating produced by a high-powered ground based transmitter. Our progress in analysis of the Secede and Ionospheric Modification data is described and the results are discussed. We shall first present the analysis of our Fabry-Perot interferometer data from the Secede III barium release series in Alaska, 1969. Then we shall describe the improved Fabry-Perot apparatus developed for the Secede II series at Eglin, Florida, 1971 and the first-look at some of the data obtained with our instrument. Finally, we shall present the results obtained with our spatial-scanning photometer used in conjunction with the Boulder Ionospheric Modification Experiment in 1970 to detect electron heating in the F region.

## II. Secede III Data Handling and Analysis

### A. Data Handling

A 45 mm aperture Fabry-Perot interferometer which we had developed for auroral studies was pressed into service on short notice for the Secede III observations by the addition of a reasonably accurate ( $\sim 1$  milliradian) pointing head, control and data processing electronics, 4-channels of Brush chart recorders to present data in real time, and a 4-track 1/4" magnetic tape recorder, two tracks recording instrumental data and two tracks recording comments of the optical pointing operator and of the electronics console operator. Figure 1 shows a sample of the real time data obtained from the Brush records. Channel 4 shows the cyclical pressure scan (corresponding to wavelength scan of the spectral line), the pulse at the midpoint denoting a filter change from the  $\lambda 4934$  ion line to the  $\lambda 5535$  neutral line (the two lines were scanned sequentially).

Channel 9 is the D/A output of the line profile scanned in a single pass, while Channel 2 is the line profile accumulated in a multi-channel memory after a number of passes. Channel 7 is the integrated line intensity of the  $\lambda 4934$  and  $\lambda 5535$  lines obtained in a monitor channel (one D/A overrun is apparent midway in the record). The instrument obtained useful data on most of the releases; however reduction of the real time records was very slow and laborious (the details of this data reduction are given in Section IIB), and the 1/4" magnetic tape records were not in a form compatible for computer-assisted reduction.

As part of the present contract, interfacing was constructed to transform the pulse train data on the 1/4" tape in 2 stages, first to 1/2" magnetic tape in an intermediate form, and then to another 1/2" magnetic tape in a word form suitable for reading by a computer (instructed by an appropriate program that was developed for the purpose). This interfacing device was used to transcribe the GUM release interferometer data (evidently the most interesting release in the series); this 1/2" magnetic tape record can be made available on request to contractors in need of the information for Secede III analyses. However, transcription of the single record took about one month, since the transcriber must listen to the audio tracks to note event occurrences, generate file marks, and prepare a log to correlate all of the data inputs. For example, boresight camera pictures were taken at varying intervals and with various exposures. Pointing information is on the audio track

in verbal form and in the boresight photographs. Thus, the point in the ion or neutral cloud at which a particular spectral line shape was taken is determined by a study of the Brush recorder charts (with real-time annotations added in longhand), the audio tracks and the sequence of boresight photographs. From this an event mark is added to the 1/2" magnetic tape and an entry made in the log noting time and pointing information. As a result of the inherent inefficiency of this process we did not transcribe other Secede III events to 1/2" magnetic tape, since other tasks of the contract took priority.

## B. Secede III Data Analysis

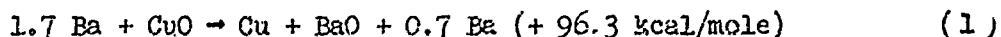
### 1. Background Information

The 45 mm aperture Fabry-Perot was operated from Ester Dome Observatory near Fairbanks, Alaska to observe the Secede III barium releases in February and March 1969. A brief survey of the purpose of the releases and a summary of cloud morphology will serve to introduce the problems we have attempted to attack in the data reduction.

Historically the first barium releases were conducted by a group at the Max Planck Institute for Physics and Astrophysics<sup>1, 2, 3</sup> for providing information on interplanetary electric and magnetic fields. Their preliminary tests were conducted in the ionosphere and in addition

to evaluating different release techniques, gave information on ionospheric electric and magnetic fields and neutral winds. Subsequent efforts by groups in the United States<sup>4</sup> have been directed toward using the barium plasma as a probe to test ionospheric properties and to attain an understanding of the development of plasma instabilities in the cloud. For these studies the distribution of ions in space must be determined. Since it is also desirable to achieve the highest possible release efficiency (ionizable barium), observations of the evolution of the neutral species are of interest.

The barium releases are achieved by igniting a thermite-type reaction in cannisters sent aloft in carrier rockets. The cannisters contain Ba and CuO in a molar ratio of 1.7:1. The reaction:



provides neutral atomic barium, and enough energy to eject a spray of superheated liquid reaction products from the cannister. Neutral barium is the most volatile reaction component and is vaporized from the droplets. The first ("snowplow"\*) phase of the cloud expansion is extremely rapid (radial expansion velocities on the order of 1 km/sec) until the expanding gas has swept out a mass of ambient significant compared to the mass of released gas. This takes a time on the order of 0.5 sec., depending on the size of the release. The expansion then slows down as the mass of the swept-up ambient gas becomes large compared to the mass of released gas. It can be expected that during this period

---

\*By a snowplow expansion we imply an expanding "solid" sphere which drives the ambient atmosphere outward.

the ambient atmosphere (which had been excluded from the sphere of expanding reaction products during the first phase) will begin to intermingle with the expanding barium vapor. The second phase gradually degenerates into a purely diffusive expansion of Ba vapor in the ambient atmosphere. The cooled liquid droplets then continue outward on a ballistic trajectory, leaving behind a sphere of neutral barium vapor. The expanding particulate sphere has no further effect on cloud morphology after the atomic barium has been vaporized. The release must be made under solar illumination for an ionized cloud to be produced, and optical observation of the cloud requires a reasonably dark sky background. As a consequence the releases are done during late twilight or just before dawn. In the absence of significant cloud drift about twenty minutes of observation are possible in either case.

Creation of the major portion of the ionized barium involves a two-step photoionization process. Figure 2 shows partial energy level diagrams for neutral and ionized barium (BaI and BaII). Ground state neutrals are first pumped (by solar radiation or thermal collisions) into the  $^1D_2$  and  $^3D_{3,2,1}$  metastable levels. From these levels they are then ionized by solar radiation. The maximum wavelength for ionization of the  $^1D$  metastable is  $\lambda 3265\overset{\circ}{\text{A}}$ , where the solar flux is approximately thirty times<sup>3</sup> that at  $\lambda 2300\overset{\circ}{\text{A}}$ , which is the approximate maximum wavelength which can lead to ionization of ground state barium. A prime argument for the validity of the two-step photoionization process has been that strontium releases provide no ion cloud, despite the fact that the strontium term diagram is qualitatively similar to barium. The major difference is that the  $^3D$  level in Sr is not metastable, and the  $^1D$  metastable does not



appear to be pumped, perhaps because of its proximity in energy to the  $1p_0$  level.<sup>2</sup>

Creation of the major portion of the ion cloud occurs within one or two minutes of release. Rosenberg et al.<sup>4</sup> give a time constant for ion creation at 170 km of close to 10 seconds. After that, however, ions continue to be created from the neutral cloud at a slow rate, creating a tenuous "ion-bridge" in the space between the separating ion and neutral clouds.

Separation of the main clouds is caused partly by neutral winds carrying the neutral cloud away from the ion cloud which is locked to the magnetic field. Also any electric fields which are present will result in  $\vec{E} \times \vec{B}$  motion of the ion cloud but not the neutral cloud. The neutral cloud motion has been used for mapping winds, and the ion cloud motion for detecting electric fields, especially noticeable in the auroral zone. Mapping of density in the clouds by standard optical techniques (filter photography, filter photometers, spectrometers) is greatly complicated by the resonant nature of the optical transitions used for detecting the cloud. Trapping of this resonance radiation destroys the simple linear relation between intensity and line of sight density which would hold in an optically thin scatterer. Consequently estimates of total inventory by calibrated photography or photometry will be too low.

We have used the Fabry-Perot to measure the shapes of the spectral lines. These measurements, combined with calculations of how the line shape depends on line of sight density, give a much better picture of actual neutral and ionized barium density distributions in the clouds. The problems to which we have addressed ourselves are: the determination

of Ba I ground state density from the  $\lambda 5535$  line, important for cloud morphology and release kinetics; the Ba I( $^1D_2$ ) metastable density from the  $\lambda 5826$  line, bearing on ion production; and the Ba II ground state and metastable state densities from the  $\lambda 4934$  and  $\lambda 6142$  lines, important for characterizing the ion cloud.

The calculations of resonance radiation transport necessary for interpreting the neutral line shapes draw heavily on the theory developed by Thomas<sup>5</sup> and are described in Appendix A. Briefly, we have assumed a Gaussian radial distribution of neutral atoms, expanding only by diffusion with a diffusion coefficient of  $0.05 \text{ km}^2/\text{sec}$  (measured by AFCL<sup>6</sup> on the Puerto Rico releases at 188 km). Although there is considerable hyperfine structure in all the barium lines due to isotope and nuclear spin effects, Table I shows that the magnitude of the splitting is negligible compared to doppler temperature broadening except in the  $\lambda 4934$  Ba II line. Accordingly for the  $\lambda 5535$  radiation transport calculations we have assumed a single frequency, thermally broadened line shape in a two level (ground state and excited state) approximation. Further approximations are discussed in Appendix A.

Line shapes were obtained on all six releases of the Alaska series, but data from only one event has been reduced at present. This release, event "Gun", is of interest because it was similar in size and altitude to event "Dogwood" of the Puerto Rico series. It is hoped that comparison of the two events will be of interest in comparing differences in response of artificial plasma clouds to the arctic and tropic ionospheric conditions.

TABLE I

Intensities and wavelength shifts for hyperfine components of barium lines.<sup>11</sup>

Mass	5535		6142		4934	
	Int	$\Delta\tilde{\nu}$ (mK)	Int	$\Delta\tilde{\nu}$ (mK)	Int	$\Delta\tilde{\nu}$ (mK)
138	71.66	0	71.66	0	71.66	0
136	7.81	+ 6	7.81	+ 6	7.81	+ 6
134	2.42	+ 9	2.42	+ 9	2.42	+ 9
137	1.87	-16	6.36	- 5	3.53	-123
	3.74	- 6	4.94	+11	3.53	- 72
	5.61	+16			0.71	+146
					3.53	+197
135	1.10	-10	3.71	- 5	2.06	-105
	2.20	0	2.89	+ 8	2.06	- 60
	3.30	+23			0.41	+136
					2.06	+180

NOTE - The splitting of the  $\lambda 5535$  line would not be completely masked by a thermal doppler FWHM of 33 mK for barium at 900°K, but we would not expect it to be noticeable with our resolution and signal-to-noise, as was the case.

## 2. Neutral Cloud - $\lambda 5535\text{\AA}$ and $\lambda 5826\text{\AA}$

Figure 3 is a plot of the optical depth effects observed in  $\lambda 5535$  for event Gum. As in studies of the OI lines, the quantity we have used for analysis is the contrast half-width of the line shapes, i.e. the full width at an intensity halfway between the maximum and minimum in the profile. In determining the contrast half-width the experimental points have been fitted to a curve using the first half of the procedure detailed in Appendix A. The fitted curve (before deconvolution) has then been used to determine the contrast finesse (FSR divided by contrast half-width). The family of curves in Figure 3 has been obtained from the resonance radiation transport calculations described in Appendix B. Each curve represents the evolution of a constant inventory, constant temperature neutral barium cloud in time with diffusion the only "loss" process. Instrumental broadening has not been removed from the experimental half-widths, so that the computer generated resonance profiles have been convolved with the appropriate instrument function before computing the half-width. The computational temperature used for the family of curves in Figure 3 is  $500^\circ\text{K}$ , which is the temperature at 1.0 km given by the USSA (Supl.)<sup>7</sup> model atmosphere for winter and an exospheric temperature of  $1260^\circ\text{K}$  (obtained from the Jacchia satellite drag model mentioned earlier with the parameters for Fairbanks at 05:20 UT, March 19, 1959;  $\bar{F}_{10.7} = 155$ ,  $F_{10.7} = 197$ ,  $K_p = 1$ ). One curve was also run for  $T = 750^\circ\text{K}$  to show how the inventory would change if a different cloud temperature were appropriate. The deduced inventory at  $750^\circ\text{K}$  is approximately 1.5 times the inventory at  $500^\circ\text{K}$ . The deduced inventory for a  $900^\circ\text{K}$  cloud at middle and late times is constant and equal to 0.3% of the total vaporizable barium available in the release.

If the neutral barium temperature does not change substantially, Figure 3 suggests a sharply falling neutral inventory in the early moments of the cloud history when ionization of the neutrals is occurring. The magnitude of this fall is somewhat deceiving. If the initial values are taken seriously they indicate a total Ba I inventory of close to  $7 \times 10^{25}$  atoms, compared to the maximum observed yield of 20%, or  $1.3 \times 10^{25}$  atoms. Therefore either the transport calculations are in error or some of the observed  $\lambda 5535$  broadening must be produced by the temperature of the neutral barium being substantially in excess of the  $900^\circ\text{K}$  ambient atmospheric temperature.

We have considered the possible distribution of the excess energy in Reaction (1), i.e. 96 kcal/mole. Föppl et al.<sup>3</sup> require 60 kcal/mole to bring the liquid expelled from the cannister (reaction products plus excess barium) to  $\sim 2000^\circ\text{K}$ . The remaining 36 kcal/mole is then available for vaporizing the excess (atomic) barium,\* heating the vaporized barium above  $2000^\circ\text{K}$ , heating the entrained and/or penetrating atmosphere, and driving the initial cloud expansion. If we assume a 20% efficiency of vaporization of the excess barium (the maximum according to measurement<sup>3, 4</sup>) then 31 kcal/mole remain for heating and expansion. In event Gum, which contained 48 kg of reactants with composition appropriate to Eq. (1), we arrive at a total of  $4.7 \times 10^3$  kcal ( $2 \times 10^{14}$  ergs). At an ambient pressure of  $3.5 \times 10^{-3}$  dynes/cm<sup>2</sup> at 170 km (USSA Suppl.,  $T_{\text{exospheric}} = 1260^\circ\text{K}$ , winter model) the initial "snowplow" expansion to a radius of 1 km requires only  $1.5 \times 10^{13}$  ergs to displace the ambient atmosphere, i.e. less than 10% of the available energy.

---

\*Latent heat of vaporization of Ba is 36 kcal/mole at  $1910^\circ\text{K}$ .

The energy required for the second and slower expansion phase (which degenerates into the diffusion phase), as well as the energy consumed in heating the interdiffusing ambient atmospheric species, depends on how effective the hot barium vapor is in continuing to drive back the ambient atmosphere. Models of the early expansion period are under investigation by AFCRL (Reference 8, p. 5) and W. B. Murcray of the University of Alaska (Reference 8, p. 97).

We have been discouraged from pursuing further cloud calculations on the basis of simplified models of pure adiabatic snow/low expansion or complete mixing for the following reasons. Adiabatic expansion with no mixing could enlarge the cloud only to a radius of 2.5 km with the energy available ( $2 \times 10^{14}$  ergs), after which the expansion would be by diffusion and would increase the cloud radius relatively slowly ( $\sim 200$  m/sec). However, the cloud is observed to grow to a 5 km radius in the first 5 seconds before diffusion takes over. Alternatively, a complete mixing model would require complete sharing of the excess energy with all ambient species in the initial 5 km sphere. This would result in a temperature rise of only  $\sim 50^\circ\text{K}$ . But there is certain to be some pre-heating of the surrounding atmosphere by the outgoing liquid droplets, and some interior volume of the sphere is certain to be evacuated by the

initial (fast) expansion. Thus neither simplified model appears to be refined enough to even estimate what the barium temperature should be after the cloud has expanded to 5 km.

Common sense would suggest that at least the interior of the cloud would remain at an elevated temperature for some time after initial expansion. If this is the case then the narrowing of the experimental  $\lambda 5535$  lines with time would involve both a depletion of neutral inventory (through ionization and oxidation) and a cooling of the cloud (by conduction and intermixing). The time constant for conductive cooling of a 1 km sphere of Ba and  $Ba^+$  at  $2500^\circ K$  grading to a  $900^\circ K$  ambient temperature at 5 km is initially between 10 and 100 seconds depending on density inside the sphere ( $10^7 \text{ cm}^{-3}$  -  $10^8 \text{ cm}^{-3}$ ). The time constant for diffusive intermixing should be of the same order of magnitude, based on the observation that the Ba cloud expands radially at roughly 200 m/sec when it is 5 km in radius. Whether a refined cloud expansion model could allow as high an initial temperature as we seem to observe must await the results of the calculations mentioned above.

Figure 4: is an attempt to assess the competing effects of resonance absorption and atom temperature on the line profiles. In it an experimental line shape obtained 45 seconds after release has been compared with two computer generated profiles having the same half-widths but different combinations of temperature and neutral density. The experimental curve has been folded about its midpoint to make the distribution of experimental points more continuous. The computed profiles are appropriate to a cloud of 5 km initial radius (measured value appropriate to  $R + 5 \text{ sec.}$ ) having undergone 45 seconds of diffusive spreading. It is

seen that a very good fit is provided by a curve with a ground state inventory of  $2.8 \times 10^{23}$  (which is near the value indicated in Figure 3 for late times) and a temperature of  $2000^\circ\text{K}$ , substantially above the expected ambient temperature of  $900^\circ\text{K}$  for this altitude. It thus appears that by very early times the bulk of neutral depletion, i.e. ionization and oxidation, may have taken place, and that subsequent ionization produces a negligible drain on the neutral inventory. The rapid decrease of line width indicated in Figure 3 seems to be caused almost entirely by cooling processes. The fact that, after 5 minutes, the data follow a constant temperature, constant inventory model curve suggests that, if continued conversion of Ba to BaO is taking place, it must be accompanied by a back reaction which replaces free barium as fast as it is lost. It should be noted that the effect of using different instrumental defect functions in generating the predicted curves in Figure 4 has been investigated and found to be insignificant.

The physical parameter which is most questionable in these calculations is the temperature. Figures 3 and 4 have shown that the inferred neutral inventory is very sensitive to the choice of temperature of the radiating atoms. It can be safely assumed that at late times the cloud has reached the temperature of the ambient atmosphere, so that the constancy of the neutral inventory at late times is justified. One way of determining the temperature independently would be from the rotational structure of the BaO bands observed in the release. Since in another experiment a spectrometer was observing these bands (Reference 8, p. 86) during the Gum event, it may be possible to obtain the desired information in the near future.



Such temperature measurements from BaO bands have been reported by Harang and Stoffregen<sup>9</sup> from Ba releases by the Max-Planck-Institute. They recorded BaO temperatures at R+1 minute appropriate to undisturbed atmospheric temperatures. They do not specify the size of the releases, but typically the Max-Planck releases are smaller than Gum by a factor of 50. Such a small release would tend to equilibrate much faster, so that the Harang and Stoffregen measurements do not necessarily apply to early times of the large Alaska releases.

Without knowing the distribution of BaO within the cloud, it would be hazardous to apply BaO temperature measurements to the question of whether the cloud temperature is high enough to thermally populate the metastable levels. If the BaO is generated by the ambient atmosphere as it penetrates and cools the outer reaches of the cloud, then the BaO temperatures would be much lower than the interior temperature of the cloud where ion generation is taking place. Thus a low BaO temperature would not necessarily contradict a high interior temperature, whereas a high BaO temperature would support it. The BaO measurements can therefore only be treated as a lower limit to the interior cloud temperature.

Another method of determining the cloud temperature would be to determine the width of the  $\lambda 5826$  metastable line at very low intensity so that optical depth effects are negligible. This method has the advantage that it gives the temperature at the location in the cloud where the metastable level is being populated. Unfortunately the profiles we obtained of the  $\lambda 5826$  line are entirely too noisy for this purpose.

Instead of determining the exospheric temperature as we have done for Gum by using measured decimeter flux and magnetic index values in

conjunction with Jacchia's satellite drag model, it would be more accurate to use the interferometer to measure the exospheric temperature from the OI  $\lambda 6300$  line sometime during the course of the cloud evolution. In either case the exospheric temperature must be extrapolated to release altitude through a model atmosphere, but the measured red line temperature would remove at least one uncertainty. In practice, accumulating a reasonable red line profile would probably take sufficiently long that it would be preferable to accumulate the red line after the barium cloud has disappeared and then extrapolate backward in time using the Jacchia model.

One comparison that has proven interesting in all the barium lines is between the line intensity at the peak of the Fabry-Perot profile, the integrated FP profile intensity and the integrated line intensity which comes through the monitor. In Figure 5 the  $\lambda 5535$  data points show the measured time variation of these quantities. Also shown are the variations predicted by the computer solution for a  $900^\circ\text{K}$  diffusing cloud of constant inventory  $2 \times 10^{23}$  atoms. Two things are especially striking about this plot. The first is the rapid initial decline of the monitor intensity which is not matched by the FP peak intensity. Our first impression was that this resulted from contamination by BaO bands. Brown (Ref. 7, p. 86) has detected an interfering band in a spectrum taken during the first 40 seconds of Gum, but published no intensities. When the FP profile is integrated over the line, however, the square points in Figure 5 result, indicating that no major contamination by BaO is present. It is our present feeling that the initial rapid fall of the monitor and integrated FP  $\lambda 5535$  intensities is linked to the high

initial temperature during the creation of the bulk of the ions. Although analyses similar to Figure 4 will be applied to all the early profiles in an attempt to separate the cooling effect from the ionization effect, it is not expected that these analyses will be too successful. The reason is apparent from looking at the scatter of points near the peak of the profile in Figure 4. Much depends on the placement of the peak intensity, and the scatter is too large to do this with any great certainty. In future releases we will attempt to obtain a better early time history of the  $\lambda 535$  line profiles.

Even with the data in preliminary form, however, a question is raised with respect to the two-step photoionization. Since the BaI inventory remains stable for a long period of time even under solar illumination as intense as that flux responsible for the initial ionization and since the main ionization is produced initially when the plasma is very hot, it appears that the high temperature of the barium cloud is more efficient in populating the  $1,3D$  metastable levels than solar pumping. In fact if thermal equilibrium were established at  $2500^\circ K$ , a reasonable temperature in very early time, the  $3D$  levels which lie 1.13 eV above the ground state and together have a statistical weight of 15 would contain 7.3% of the total neutral inventory, and the  $1D$  level with statistical weight 5 which lies 1.44 eV above the ground state would contain 0.6% of the neutral inventory. To our knowledge the thermal population of metastable levels has not been considered previously as the major source of metastables which are subsequently photoionized.

The second striking feature of Figure 5 is the continued and rapid decline of intensity of the monitor and FP peak at times when the

cloud model predicts much less of a decline for both of those quantities. If the cloud maintains a constant neutral barium inventory throughout its diffusive expansion (as the recorded profiles suggest), then even at  $R + 18$  minutes (0537) the cloud has an optical thickness of 2.5 and is scattering all the sunlight incident upon it. The model then predicts a very modest decline in peak intensity. If our interpretation of the profiles is correct, then the falling intensity must result from a decline in the exciting solar flux caused by atmospheric scattering. Since the last data point at  $R + 18$  minutes was taken just before the neutral cloud vanished (when the earth's shadow height reached 170 km) this interpretation seems reasonable for very late times. On the other hand, whether one would expect to find a decreasing solar flux irradiating the cloud at early times must await more accurate determinations of the cloud height from triangulation, as well as numerical calculations of atmospheric scattering. Results of a detailed calculation of atmospheric attenuation have been published by Lloyd<sup>10</sup> and will be applied when cloud position data become available. A crude graphical calculation (ignoring refraction effects) shows that at release time the solar flux illuminating the cloud passes only 40 km above the surface of the earth and this height decreases by  $\sim 2$  km per minute.

The observation of steady neutral Ba inventory despite falling line intensity from the cloud exhibits another shortcoming of photometric observations, i.e. that in developing a time history of the cloud the time dependence of the illuminating intensity must be known, whereas

the density determinations from line shape observations are insensitive to the intensity of the flux.

Figure 6 shows the time variation of the FP and monitor intensities of the  $\lambda 5826\text{\AA}$  line which has the  $^1D_2$  metastable state as a lower level. The abrupt change in slope coincides in time with the break observed for the  $\lambda 5535$  line. The appearance of the slope transition in both wavelengths supports our belief that there are two separate processes involved in populating the metastable levels. In our model the break in the intensity curves would coincide in time with a change in the process responsible for pumping the metastable levels. We would expect a corresponding break in the intensity curves for lines terminating on the  $^3D$  levels, but occurring later in time than for the  $\lambda 5826$  line since the Boltzmann factor is less for the lower lying  $^3D$  levels and they should remain in thermal equilibrium longer with the ground state. Since the line peak intensity tracks the integrated (monitor) intensity so well, it appears that at no time is the barium cloud optically thick for  $\lambda 5826$ . An upper limit may thus be placed on the  $^1D$  density and translated into percentage of neutrals in the  $^1D$  state for given ground state densities. At  $R + 45$  seconds this limit is either  $<3\%$  or  $<60\%$ , using the ground state densities deduced from Figure 18 at cloud temperatures of  $900^\circ\text{K}$  or  $2000^\circ\text{K}$ , respectively. The difference of slopes at late times and low signal levels is assumed to be the result of contamination.

Pictures taken with the boresight camera showed that, while we were generally not pointed at the exact center of the cloud, we were less than one-quarter of a Gaussian radius away from the center. Calculations of the distortion of the  $\lambda 5535$  line profile generated by this sighting

error reveal that within one-quarter of the Gaussian radius the half-width should change less than 3%. Doubtless some of the fluctuation of the experimental points in Figure 3 is due to sighting closer or farther away from the cloud center. Since boresight pictures were not taken continuously enough to provide a complete record (1 picture every 3-4 scans at early times) we have ignored the small sighting errors and assumed in all calculations that we were aimed at the cloud center.

### 3. Ion Cloud - $\lambda 4934\text{\AA}$ and $\lambda 6142\text{\AA}$

In addition to the BaI lines  $\lambda 5826$  and  $\lambda 5535$ , measurements were carried out on the  $\lambda 4934$  and  $\lambda 6142$  lines of BaII. The  $\lambda 6142\text{\AA}$  line terminates on the  $^2D_{5/2}$  metastable state of  $\text{Ba}^+$  and we had planned to obtain metastable densities by observing optical depth effects.

Unfortunately the FP spacer was adjusted for the Gum release so that in scanning, less than half a  $\lambda 6142$  profile was recorded, making interpretation impossible. The  $\lambda 6142$  monitor intensity was comparable to  $\lambda 4934$ , so that density estimates should be possible on other releases of the series where the  $\lambda 6142$  line placement in the FP scan was more favorable.

As shown in Table I (p. 9,) the  $\lambda 4934$  ion line is the only one of the four lines observed where the hyperfine splitting is large enough to noticeably affect the line shape. Using the values of the splittings and relative intensities given in Table I (obtained from Kivel et al.)<sup>11</sup> a line shape was generated for an optically thin  $\lambda 4934$  source at  $800^\circ\text{K}^*$  and convolved with an instrumental function appropriate to late time observations

---

\*The choice of  $800^\circ\text{K}$  for the  $\lambda 4934$  computational ion temperature was an estimate made during preliminary data reduction. The heuristic nature of Figure 7 does not justify the effort of recomputing the profile and re-drawing the figure with a more accurate temperature of  $900^\circ\text{K}$ .

of the ion cloud. This profile is shown in Figure 7 along with a profile observed at R + 26 minutes in Gun. A complete profile extends from the values 52 to 173 on the arbitrary frequency scale; partial profiles from the interference order before and after the complete profile are also shown. The eleven hyperfine components have been combined into 3 groups of closely spaced lines with centers of gravity indicated by the arrows labeled with each group's relative intensity. The thermal doppler broadened profile of the isolated component on the left of the main component is decoupled from radiation in the main peak and will henceforth be referred to as the "hyperfine line". The experimental shape has been normalized to the peak of the hyperfine line and the minimum to the left of the hyperfine line of the theoretical profile. It is obvious that even at such late times in the cloud history there is substantial absorption of the main component, and that such absorption will lead to erroneous estimates of line of sight ion densities from photometry and photometric photography. For an optically thin medium the ratio of the intensity of the main peak to the hyperfine peak should be 14.7. At late times this ratio approached 10 in the ion cloud, indicating an optical depth of about 0.9 for the center of the main component, or a line of sight density of about  $1.5 \times 10^{11}$  ground state ions per  $\text{cm}^2$  (see Appendix A for relation between main to hyperfine ratio and optical depth).

Figure 8 shows the time variation of the monitor (integrated total intensity), the main peak, and the hyperfine peak intensity of the  $\lambda 934$  line. It appears that the hyperfine intensity rather quickly attains a steady (exponential) decay rate which is only reached at a much later time by the main peak intensity since our earlier resonance

radiation calculations have shown that an optically thick scatterer should give a reasonably constant intensity, it is our impression that the main component decay must be largely due to the falling solar flux intensity.

The large scatter of data points around the fitted curves in Figure 8 is caused by slight pointing changes with respect to the fine striations in the ion cloud. At about R + 6 min. for Gum the rf returns underwent a change in nature (Ref. 8, p. 175) from what would be expected of a single scattering object to a multiple object. This time coincides reasonably with the visual change of the ion cloud from a smooth to a striated shape; looking eventually not unlike a rayed auroral arc, but lacking the rapid internal motion characteristic of a rayed arc. Early in time the ion cloud may be characterized rather easily by a diffusion model with different diffusion coefficients parallel and perpendicular to the magnetic field and ion density decreasing monotonically. Prior to striation the ion density appears to begin to increase again<sup>12</sup> until the plasma instability takes over completely and partitions the ion cloud into a multitude of filamentary bundles. For Gum the FP was pointed at the region of peak ion light intensity from roughly 40 seconds before striation (as determined by the appearance of multiple returns from the SRI short pulse radar (Ref. 7, p. 175)) until some minutes later. The individual scans of 1494 will be investigated very thoroughly when complete reduction of the barium data is undertaken to obtain ion column densities prior to and just after striation. The chief difficulty with analysis of the Fabry-Perot data is that we have no idea of the scale of the structure in the



line of sight, so that column densities may not be easily converted to volume densities, the quantity of interest for comparison with rf measurements. This problem is particularly bothersome after striation, when the scale of the structure may be even smaller than the acceptance cone of the FP. Integration over several filaments which have voids between would give us a lower estimate of ion densities than would actually be present.

The problem of estimating peak densities and structure scale in the striated ion cloud is now under attack using the hyperfine line. A new Fabry-Perot is under construction for use on the Secede II barium releases which will be matched to a 4-power fore telescope to give 4 minutes of arc ( $\frac{1}{2}$  m rad.) angular resolution. This is equivalent to 100 meter resolution at a slant range of 200 km. With the chamber pressure fixed at a point in the scan corresponding to the peak in the hyperfine line, a spatial scan will be executed across the striations. This will tell us the ion cloud fine scale striation structure via a line with an absorption coefficient per atom which is  $1/15^{\text{th}}$  that of the main line.

If we are willing to consider a 20% deviation from the linear relation between the h.f. line intensity and column density as referring to a medium which is "optically thin", then it should be possible to quantitatively characterize the barium ion cloud at points in its time history when the main to hyperfine ratio is as low as 1.5. According to the fitted curves in Fig. 7 this occurs at  $R = 9$  minutes, shortly after striation. However, there is a single point, which may represent a look at the middle of a striation, at  $R = 10$  minutes where the ratio is less

than 2.5. Thus we may have to take care in interpreting the spatial scans. With the instrument calibrated for absolute intensity and interspersing spatial scans with spectral scans to tell us what the main/hyperfine ratio is for a given hyperfine intensity, we should be able to make approximate corrections for optical depth in the hyperfine line. For a release the size of Gum, the hyperfine line should not exceed optical depth unity except for very early times in the formation and diffusive expansion period.

The farthest we can presently take the analysis of the Alaska data is to obtain an estimate of peak column densities of ground state ions. This comes most easily from the use of Figure 11 in Appendix A relating to the interpretation of the main/hyperfine ratio. The metastable population must be considered also; Duell and Sears,<sup>13</sup> from a consideration of transition probabilities and solar flux, estimate that  $\frac{1}{3}$  of the ion population is in the  $^2D_{5/2, 3/2}$  metastable levels (c.f. Figure 2). Furthermore the ion clouds are aligned with the magnetic field and hence are aspect sensitive. When photographic determinations of the size of individual striations become available, we will attempt to generate ion densities to compare with rf measured electron densities. This must be done with extreme care because in addition to observing the striations from an aspect other than normal to the field lines, we could be looking through several striations, or at some striations which are partially shielded from the sun by others, with a resultant distortion of the uniform solar flux. If the ion cloud were a picket fence, analysis would be straightforward. Photographs looking up the magnetic field lines show that it has more the appearance of an auroral corona. For

these reasons, obtaining ion densities from optical depth measurements is very hazardous, and has not yet been attempted in data reduction for the Alaska releases.

Alternatively it is possible to go in the other direction and to use the rf  $n_e$  measurements to derive an effective structure size which would apply if we were looking at only a single uniformly-illuminated striation. For instance at R + (10 min., 20 sec.) the main/hyperfine ratio was 2.5, implying a ground state column density of  $1.3 \times 10^{12}$  ions/cm<sup>2</sup>. This gives a total (ground state plus metastable) ion column density of  $3.2 \times 10^{12}$  cm<sup>-2</sup>. Considering that our viewing aspect to the field lines was about 40° (estimated at present; more accuracy will come from triangulated cloud positions), the ion column density normal to the field lines is  $2 \times 10^{12}$  cm<sup>-2</sup>. At this time the rf  $n_e$  values<sup>7</sup> are  $3.2 \times 10^6$  cm<sup>-3</sup> (Raytheon, HF and VHF),  $1.8 \times 10^6$  cm<sup>-3</sup> (SRI, Homer step sounder) and  $1.1 \times 10^7$  cm<sup>-3</sup> (SRI, Kodiak step sounder). Thus the single structure size that this type of analysis would indicate at R + 10 min. is  $\sim 2 \times 10^{12} / 4 \times 10^6 = 5 \times 10^5$  cm or 5 km. This seems extremely large for a single striation and must represent the sum of several striations.

The final type of information which can be obtained from FP profiles is drift velocities of the various clouds. The only occasion we have had to examine our Alaska data for such effects was when it was mentioned<sup>14</sup> that the event "Elm" ion cloud appeared to be moving westward at supersonic velocities. From a rough look at the real-time chart records we confirmed the magnitude and time dependence of velocity for the Elm ion cloud as deduced from the University of Alaska TV tracking

system. Velocity information is inherent in all our records of both neutral and ion cloud, with a velocity resolution of  $\sim \pm 30$  meters/second for the better line profiles. These drift velocity determinations give information on electric fields and neutral winds. But since cloud drift can so easily be obtained from the TV tracking or all sky camera systems, and since we have many other problems which only the FP can solve, we probably will not investigate the velocity data further.

### III. Secede II Apparatus Construction, Field Observations, and Initial Data Reduction

#### A. Apparatus

As noted in the previous section, a larger (100 mm aperture) Fabry Perot interferometer in a high-stability mounting cage was to be fabricated for use in conjunction with a 16" (4X magnification) telescope to provide high spectral resolution at higher optical speed and better spatial resolution (1/2 mrad, or 100 meters at 200 km slant range). Also, electronic data processing to provide real-time transcription of the data onto 1/2" magnetic tape in a format which could be readily reduced with computer assistance was a requirement of the new apparatus. The Fabry-Perot optical interferometric system and the electronic control system for the instrument were developed by our group at the University of Pittsburgh; the 16" telescope pointing system for the Fabry-Perot, bore-sight TV and videotape recorder, and the electronic data transcription systems were developed by General Electric Space Science Laboratories, Valley Forge, Pa.

In order to maintain parallel alignment (to  $\sim 1/100$  wavelength) of the Fabry-Perot plates during the inevitable accelerations and vibrations associated with operation on the telescope training mount, a special invar mounting cage was constructed which employed controlled deformation of very rigid structures to achieve and maintain plate parallelism. This design was modified somewhat from the original version in order to improve the smoothness of the parallelism adjustment. In addition, a wavelength sensitive beam-splitting mirror and dual detection head was attached to the output stage of the interferometer to permit simultaneous scanning of two spectral lines (as opposed to the sequential line scanning system of the Alaska instrument) without loss of light in either channel. In this instrument, a separate, boresighted monitor filter photometer was added to provide

total intensity records of the various lines ( $\lambda 4934$ ,  $\lambda 5575$ ,  $\lambda 6111$ ,  $\lambda 6142$ ) observed by the interferometer.

An electronic control unit making extensive use of integrated circuits was constructed to permit flexible operation of the interferometer in the wavelength scan and wavelength-lock (spatial scan) modes, e.g., variable rate of scan, dwell-time per channel, number of channels per scan. In addition, remote control of all changes at the interferometer (such as filter selection;  $\lambda 5535$  &  $\lambda 4934$  in one channel;  $\lambda 6328$  [laser calibrator],  $\lambda 6142$  and  $\lambda 6111$  in the other) was provided. The output pulses of the three detecting photomultipliers were fed to specially designed preamplifier, discriminator, wave shaping and cable driving circuits to provide standard pulses for the data processing circuits built by G.E.

#### B. Field Observations

The final integration of the Fabry-Perot with the telescope augmented pointing system took place at the field site S-3a ( $30^{\circ} 6'N$ ,  $85^{\circ} 14.2'W$ ) at Wawahitchka, Fla. The optical interferometer systems functioned properly, achieving a detection sensitivity very close to that predicted for the Secede II releases on the basis of our Secede III Alaskan observations. Most of the difficulties in the field occurred with the spatial scan computer which controlled the mount pointing, with the boresight TV/videotape system, and the digital magnetic tape data recording system.

These deficiencies were corrected sufficiently well by the time of first release that good data was obtained on all twilight-nighttime releases (with the exception of Nutmeg, where only the real-time Brush recorder records were obtained, owing to failure of the digital magnetic tape data system; the videotape recorder failed on both Nutmeg and Plum). The

rationale behind the Secede II field observations, together with a preliminary analysis of some of the data, is given in the next section.

### C. Initial Secede II Data Reduction

#### 1. Introduction

Observation with Fabry-Perot (FP) interferometers on barium releases in Alaska<sup>15</sup> and Puerto Rico<sup>13</sup> have shown that the  $\lambda 4934$  line profile is severely distorted by optical depth effects. These effects give rise to a relationship between source brightness and line-of-sight ion density which is unknown because of non-uniform source excitation. This means that photographs taken in the light of such an optically thick transition do not provide reliable quantitative information on absolute or relative ion column densities.

Line profiles from the Alaskan series<sup>15</sup> suggested that a subsidiary component of the  $\lambda 4934$  line which is well removed from the main peak becomes optically thin quite soon after release (1-3 minutes). This subsidiary component, hereafter referred to as the hyperfine (hf) line, was expected to be uniformly excited in the cloud and provide reliable quantitative information on ion column densities. Thus an instrument (described in the preceding section) was constructed which was capable of isolating this component and performing angular scans across the ion cloud to provide a two dimensional map of ion column density.

#### 2. Instrumental Parameters

The large aperture (100 mm) FP<sup>16</sup> achieved an overall finesse of 20 and was coupled to a servo controlled 16" Cassegrain telescope. The telescope reduced the field of view of the FP to a point where small scale structure ( $\sim 100$  meter) could be resolved, while retaining an acceptable light gathering power. Coupled to the telescope pointing axis

were an image orthicon television camera for boresight and tracking records and a filter photometer (monitor) for recording integrated line intensities. Fields of view were: for the FP-telescope-0.76 m rad, for the monitor--1.66 m rad, and for the TV- approximately  $6^\circ$  by  $8^\circ$ . The FP was capable of being pressure scanned in wavelength, and achieved lock on the hyperfine line by closing the inlet gas valve at a selected chamber pressure. The dual detecting head permitted observations of two lines simultaneously, normally  $\lambda 4934$  and  $\lambda 6142$ . The monitor could be cycled through 4 filters ( $\lambda 4934$ , 5535, 6111, and 6142) and one dark position for dark counting rate, or could be fixed on any one of the above positions. It was normally left fixed on  $\lambda 4934$ .

Normal operation of the FP was in the spatial scan mode either at low speed to resolve fine structure, or at a higher speed to record an entire cloud profile. At release time and at intermittent times throughout the event,  $\lambda 4934$  wavelength scans were taken to calibrate the optical depth of the hyperfine line. An occasional  $\lambda 5535$  wavelength scan was taken to study the neutral cloud morphology.

In the dual detection mode the peak of the  $\lambda 6142$  metastable ion line occurred at the same FP chamber pressure as the peak of the hf line of  $\lambda 4934$ . Thus a spatial scan in 6142 light was recorded at the same time as the hf scan. While the  $\lambda 6142$  signal was not strong enough to permit detection of individual striae, the overall envelope of the cloud in  $\lambda 6142$  will provide information on the partition of the ion population between metastable and ground states.

Absolute intensity calibration of the FP and monitor was performed following each event. The source used was a  $C^{14}$  radioactive phosphor low brightness source (LBS) with calibration traceable to NBS.



Real time data was presented on a Brush chart recorder and included analog signals for chamber pressure (wavelength), FP intensity (two channels), monitor intensity, differential azimuth and elevation readouts, and several channels of coded digital information, including a one second marker referenced to WWV. The same information was also recorded in a more accurate form on a 1/2" digital tape recorder for later computer retrieval. The television display, with time, azimuth and elevation superimposed, was recorded on a video tape recorder.

### 3. Preliminary Results

The system was operational on all six events of the II series. No information was obtained on event Quince because of the high ambient light level. At this time only the chart records have been examined in detail; however, it has been determined that intelligible data do exist on the digital tapes. Analysis has been concentrated on event Spruce because the caliber of data is highest there and because it was generally the most interesting event from the standpoint of this system.

#### a. Spruce

The most pertinent question that has arisen in the II series observations concerns the extent of the optical thinness of the hf line of  $\lambda 4934$ . On the Alaskan event Gum the lowest ratio of main to hyperfine components (main/hf ratio) recorded was 2.1 at R + 5 min. A first order analysis (uniform source excitation) related this value to an optical depth near or below unity for the hf line (see Section II). All the II-series events, however, gave main/hf ratios as low as 0.3 and the ratio generally remained at or below 1.0 during most of the visible cloud lifetime. Table II shows the values recorded during event Spruce along with the spatial locations at which the line profiles were taken. The regime of ratios with

Table II

Time (after release)	hf half-width (mK)	main/hf ratio	location
1 min.	100	0.2	cloud center
14 min.	71	0.32	solidifying striation
19 min.	68	0.33	main body
23 min. 30 sec.	76	0.22	striation on eastern edge
23 min. 40 sec.	71	0.55	void on eastern edge
24 min. 20 sec.	71	1.1	western edge
25 min.	70	0.9	northern nebulosity
29 min. 20 sec.	76	3.4	off cloud
30 min.	76	1.1	on cloud

values below unity can not be treated by a first order analysis. One of the fundamental tasks these data call for is a more thorough examination of the radiation transport problem to discover the significance of these highly absorbed profiles. One clue may be that in Alaska the geometry was such that the  $\lambda 4934$  line was observed to some extent in reflection, while in Florida the line was seen much more in transmission.

Another measure of optical depth effects is the amount of broadening of a spectral feature. It is instructive to inspect the  $\lambda 4934$  profiles from this viewpoint. Figure 12 shows two profiles taken at early and middle times in the Spruce cloud's visible lifetime. Also shown as solid lines are optically thin profiles including instrumental broadening which have been adjusted to fit the hf line in half-width and height. The temperature necessary to provide the appropriate half-width for the early profile is  $4000^{\circ}\text{K}$ . This temperature is extremely large, even considering the evidence suggesting that the cloud remains at an elevated temperature ( $2000^{\circ}\text{K}$  for Gum) at times as late as one minute. In addition the profile itself suggests absorption effects, but not by as much as an order of magnitude. If indeed there is absorption the error induced is probably not more than a factor of two even at such early times. The  $1500^{\circ}\text{K}$  optically thin profile provides a surprisingly good fit to the lower experimental profile.  $1500^{\circ}\text{K}$  is high but not completely out of the question for these altitudes. A Jacchia-type estimate of exospheric temperature at that time should be made to determine just how unreasonable  $1500^{\circ}\text{K}$  is. Table II shows that the hf half-width does not change appreciably over a wide range of times and main/hf ratios in Spruce, so perhaps what we are seeing in the lower profile is a high-temperature, optically thin hf line.

Pending further study we must leave unanswered the question of the optical depth of the hf line. The remainder of this section deals with the spatial characteristics of the Spruce cloud as viewed from site 3a.

Figure 13 shows four successive spatial scans at medium speed across a portion of the Spruce cloud covering times from 00:11:58Z to 00:12:55Z. The element of emphasis in this figure is the striation indicated by the dashed vertical line. It has a half width (depending upon choice of base line) of less than the resolution of the instrument or less than about 150 meters assuming 180 km slant range. For a strong, narrow striation such as this, which showed quite distinctly on the TV presentation, the modulation depth,

$$D_M = \frac{I_{\text{peak}} - I_{\text{valley}}}{I_{\text{valley}}} \quad (2)$$

is 40% in trace 1, and 65% after the striation has expanded in trace 4. This series is a particularly good example of a well defined fine scale striation. In most cases the modulation depth for fine scale structure is closer to 10%. What appear visually as distinct striae are virtually always superimposed on a diffuse background when they occur in what was once the main body of the ion cloud.

Figure 14 is an example of a different class of effect which occurred quite often although not often so dramatically. The solid line is the hf peak intensity on a scan through the late-time Spruce cloud, and the dashed line is taken from the monitor at the same point. The curves have been normalized at the local minimum near the center, and they track reasonably well going west from that point. But the sharp

rise in the hf intensity going east is not matched at all by the monitor. Thus an instrument such as a camera or the monitor which records integrated line intensity would give an erroneous value for the ion column density. The same effect quite often shows up when scanning across a localized enhancement such as a striation. The modulation depth is greater in the hf line than in the total line as recorded by the monitor.

One of the stated objectives of this system was to track the flashing light on the rocket payload vehicles (probe and beacon) on the TV to obtain a point by point comparison of RF electron densities with optical ion densities. Only two vehicles have thus far been identified on video tape, both on event Spruce. Table III gives times during which these vehicles were observed and the operational mode of the FP surrounding those times. Exact vehicle positions will be taken from the video tape.

During most of the beacon occultation as viewed from Site 3 the FP was performing  $\lambda 4934$  wavelength scans on a developing striation near the trailing edge of the ion cloud. One of the scans is shown in the lower trace of Figure 12. At the time of the last observed flash the beacon was traversing that same striation at a point about  $2^\circ$  south of where we had taken the wavelength scan. It was some  $3/4^\circ$  into the cloud on a track running at approximately  $65^\circ$  to the striation axis.

Figure 15 shows the hf line traces of the three spatial scans surrounding the occultation. The earliest of the three (top) shows the abrupt change in slope associated with the hard edge, and the bridge trailing to the left in the figure. The middle trace shows some motion of the cloud to the left (eastward) and very little structure. Fine structure could be present but the chart records do not have enough

Table III

Event Spruce--Times surrounding vehicle observations on TV.

Time (UT)	Event
23:57:51	Begin spatial scan*
58:18	end spatial scan
58:28	begin spatial scan-through bridge and across long axis of ion cloud
58:45	acquire probe
59:02	lose probe
59:03	end spatial scan
59:23	reacquire probe
59:30	last observed probe flash
59:38	begin spatial scan
00:00:07	end spatial scan
00:35	begin spatial scan
01:02	end spatial scan
00:03:55	begin spatial scan
04:08	end spatial scan
04:19	begin spatial scan
04:46	end spatial scan
04:55	begin spatial scan
05:39	end spatial scan
05:42	acquire beacon
05:50	begin $\lambda 4934$ wavelength scan on solidifying striation
06:08.3	beacon passes visible hard edge
06:21	end $\lambda 4934$ wavelength scan
06:22	last observed beacon flash
06:25	begin $\lambda 5535$ wavelength scan on neutral cloud
06:46	end $\lambda 5535$ wavelength scan
07:07	begin spatial scan
07:46	end spatial scan
08:00	begin spatial scan
08:23	end spatial scan

\*unless otherwise noted, the spatial scans are approximately parallel to the long axis of the ion cloud through its center of gravity.

definition to be positive. The vertical bar shows the farthest excursion from the smoothed curve. The bottom trace (post-occultation) shows structure which is definite but not extremely pronounced.

At the present time absolute ion densities have not been obtained. An absolute calibration using the phosphor LBS was taken following the event but needs to be retrieved from the digital tape. Also an estimate of optical depth effects should be made before the densities can be relied upon.

#### b. Other Events

Data reduction has been concentrated on event Spruce, but some observations have been made about the general character of other releases.

Small scale (less than the FP resolution element) structure was observed on all releases except Event Olive. Striation was seen on Olive but appeared to be the preliminary large scale ( $\sim 1$  km) modulation that characterized the other clouds before fine scale structure appeared. The early  $\lambda 4934$  profiles on Olive showed line reversal at the peak of the hf line and should provide a good test of the transport theory.

On events Nutmeg, Plum and Spruce the large scale striation structure eventually divided the smooth envelope of the ion cloud into discrete groups of striations, giving a very irregular profile, as shown in Figures 13 and 14. This happened before the small scale structure became apparent. On Redwood such was not the case; the small scale structure evolved as modulation on the smooth ion cloud envelope, whose general character remained unchanged throughout its visible history. Modulation depths on the main body were typically 10%-20%. Event Olive gave indications that its evolution was following a Spruce-like course, but on a much longer time scale.

Release times of the main cloud and two of the three puffs have been taken from video tape on Olive. The main cloud appeared at 23:53:57.3Z and was followed by puffs at 23:54:06.2Z and 23:54:15.9Z, which both merged into the main cloud.

The third puff which evolved into a separate cloud showed distinct small scale structure at 9 minutes after the main cloud release. This small scale structure was gone at  $R + 18$  and only the large scale modulation remained.

The few  $\lambda 5535$  wavelength scans taken during events Olive and Spruce showed strong reversal immediately after release, but relaxed to a more thermal line shape at middle times in the cloud history. The early time line shapes will provide an excellent test for the hypothesis developed from Alaskan event Gum that the cloud remains at an elevated temperature for some time after release.

#### 4. Data Reduction

Currently, efforts have been underway to retrieve the data from the digital tapes. The form the data bank will take is planned to be a listing for each spatial scan giving azimuth, elevation, differential angle, FP intensity, and monitor intensity versus time. Requests for specific time scans can then be satisfied with a copy of the listing, or a computer drawn plot if possible. The wavelength scans will be presented as FP intensity versus pressure (wavelength).

It is planned to correlate certain spatial scans, such as in Figure 13, with photographs taken up the field lines to arrive at a three dimensional ion density model.



## APPENDIX A

### RESONANCE RADIATION TRANSPORT

For interpretation of the barium profiles recorded in Alaska, it has been necessary to develop a computer code to generate line profiles from a model of the barium cloud. For the theory of resonance radiation transport in a spherically symmetric geometry we have drawn extensively on the paper by Thomas.<sup>5</sup> This Appendix details the application of Thomas' theory to our problem.

As mentioned in the text our approach to the barium neutral cloud is to treat  $\lambda 5535$  transport as a two level process, with the upper level of the  $\lambda 5535$  line excited only by capture of a  $\lambda 5535$  photon, and decaying only through the same channel. Thus the neutral metastable states are ignored, as well as cascade to and excitation from the upper level. This approximation is probably quite good in late times when the greatest optical thickness of the cloud is about 3, but becomes more questionable in early times when the optical thickness is much higher. Further work is required to determine to what extent competing processes contaminate the two level system.

An approximation inherent in Thomas' treatment is that of complete frequency redistribution (CFR), which is that the emission coefficient and absorption coefficient are equal. A further approximation of Thomas is that both emission and absorption coefficients are Gaussian. Both of these approximations are tied together since CFR is commonly assumed to be valid (see Thomas) in the dopplercore of the line (out to 3 doppler widths from the line center). It is near this same point that the

magnitude of the natural line profile of the  $\lambda 5535$  line (natural half-width 0.3 mK, doppler half-width 33 mK) becomes comparable to the magnitude of the doppler profile. So both approximations may be accepted after one minute into the cloud history when the line width is  $2\frac{1}{2}$  doppler widths or less. Earlier than that, both approximations are suspect, but extremely laborious to investigate. In particular it would be desirable to see if a Voigt (doppler plus natural) emission profile (used in place of  $\alpha(x)$  in Eq. (A.10)) would supply enough signal in the wings of the line to affect the conclusions derived from Figs. 3 & 4; i.e. that a high temperature is required to reproduce the observed profile at  $R + 45$  sec.

Thomas has expressed the equation of radiative transfer in the form of an integral equation for the excited state density (Eq. (35) in Thomas' paper):

$$N(\vec{r}) = N^{(1)}(\vec{r}) + k_0 \rho(r) \int \frac{d\bar{\Omega}}{4\pi} \int_{\omega}^{\bar{\omega}} d\bar{s} G(\vec{r}, \vec{r}') N(\vec{r}') , \quad (\text{A.1})$$

where  $N^{(1)}(\vec{r})$  is the density of atoms excited by the primary solar radiation:

$$N^{(1)}(\vec{r}) = (J_0 / h\nu_0 \gamma) k_0 \rho(r) \pi^{\frac{1}{2}} \Delta\nu_D T(r, \omega, \bar{\Omega}_s) , \quad (\text{A.2})$$

with  $J_0$  the solar flux per unit frequency (assumed constant over the line);  $h$  is Planck's constant,  $\nu_0$  is the center frequency of the line,  $\gamma$  is the damping width,  $k_0$  is the peak absorption cross section  $\rho(r)$  is the spherically symmetric density distribution of ground state atoms,  $\Delta\nu_D$  is the thermal doppler width and  $T$  accounts for the attenuation of the

primary solar flux before reaching  $\bar{r}$ .  $T(\bar{r}, \bar{r}')$  is the probability that a photon, emitted at the point  $\bar{r}$ , will travel to the point  $\bar{r}'$  without being absorbed.

$$T(\bar{r}, \bar{r}') = \pi^{-\frac{1}{2}} \int_{-\infty}^{\infty} \alpha(x) \exp(-\alpha(x) \tau(\bar{r}, \bar{r}')) dx \quad (\text{A.3})$$

where  $x$  is a dimensionless frequency variable

$$x = (\nu - \nu_0) / \Delta \nu_D \quad (\text{A.4})$$

and

$$\alpha(x) = \exp(-x^2) \quad (\text{A.5})$$

is the (normalized) absorption and emission coefficient (equal because of CFR), and

$$\tau(\bar{r}, \bar{r}') = k_0 \int_{\bar{r}'}^{\bar{r}} \rho(r'') ds'' \quad (\text{A.6})$$

is the optical depth between  $\bar{r}$  and  $\bar{r}'$ , with the integration being carried out in a straight line.  $T(\bar{r}, \infty, \bar{\Omega}_s)$  then is the probability that a primary solar photon incident upon the medium from a direction  $\bar{\Omega}_s$ , will reach  $\bar{r}$  without being absorbed.

The second term in Eq. (A.1) represents radiation emitted at  $\bar{r}'$  and absorbed at  $\bar{r}$ . The integration  $ds''$  is carried along a line in direction  $\bar{\Omega}$ , with  $\bar{\Omega}$  integrated over all possible directions.  $G(\bar{r}, \bar{r}')$  is the (unnormalized) probability that a photon emitted at  $\bar{r}'$  will be absorbed at  $\bar{r}$ .

$$G(\bar{r}, \bar{r}') = \pi^{-\frac{1}{2}} \int_{-\infty}^{\infty} [\alpha(x)]^2 \exp(-\alpha(x)\tau(\bar{r}, \bar{r}')) dx. \quad (\text{A.7})$$

The expressions used for calculating T and G are

$$\begin{aligned} T(\tau) &= \sum_0^{\infty} (-\tau)^n / n!(n+1)^{\frac{1}{2}} \quad 0 \leq \tau < \infty \\ &= \tau^{-1} (\pi \ln \tau)^{-\frac{1}{2}} \quad 3.0 \leq \tau < \infty \end{aligned} \quad (\text{A.8})$$

and

$$\begin{aligned} G(\tau) &= \sum_0^{\infty} (-\tau)^n / n!(n+2)^{\frac{1}{2}} \quad 0 \leq \tau < \infty \\ &= (1 + \frac{1}{2} \ln \tau) \tau^{-2} (\pi \ln \tau)^{-1} \quad 8.0 \leq \tau < \infty, \end{aligned} \quad (\text{A.9})$$

where the approximations were used when the series became unstable due to computer round-off error.

Once  $N(\bar{r})$  has been determined, a line profile may be obtained by integrating along the line of observation  $\bar{\Omega}_0$ ;

$$I(x, \bar{\Omega}_0) = \text{constant} \times \int_{-\infty}^{\infty} \alpha(x) \exp[-\alpha(x)\tau(\bar{r}', \infty, \bar{\Omega}_0)] N(\bar{r}') d\bar{s} \quad (\text{A.10})$$

where the magnitude of the constant is not important since we are concerned only with shape.

Iterative techniques are used to solve (A.1) for  $N(\bar{r})$ . Two problems arise in this connection. The first is that convergence using  $N^{(1)}(\bar{r})$  as a trial solution is a prohibitively long process, since  $N^{(1)}(\bar{r})$  is generally very far from the solution  $N(\bar{r})$ . This problem is dealt with by using an approximation (c.f. Thomas) to obtain a more

accurate trial solution. If  $N(\bar{r}')$  in Eq. (A.1) is assumed constant over the region where  $G(\bar{r}, \bar{r}')$  is appreciable and taken out of the integration sign, and the equation simplified by means of an analytic relation between  $T$  and  $G$ , it becomes

$$N(\bar{r}) = N^{(1)}(\bar{r})/E(\bar{r}) \quad (\text{A.11})$$

where

$$E(\bar{r}) = \int (d\bar{\Omega}/4\pi) T(\bar{r}, \infty) = 1 - k_0 \int (d\bar{\Omega}/4\pi) \int d\bar{s} \rho(\bar{r}') G(\bar{r}, \bar{r}') \quad (\text{A.12})$$

is simply the probability that a photon emitted at point  $\bar{r}$  escapes the medium completely without being reabsorbed.  $N^{(1)}(\bar{r})/E(\bar{r})$  is then used as a first approximation for the iterative solution of (B.1). This approximation along with the preceding transport theory is discussed by Thomas.<sup>5</sup>

Our final solution does not use the iterative technique inherent in (A.1). Instead we have used Eq. (A.12) and the Born-Oppenheimer principle of expansion of an integral equation to rewrite (A.1) in the series form:

$$N(\bar{r}) = N^{(1)}(\bar{r})/E(\bar{r}) + k_0 \int (d\bar{\Omega}/4\pi) \int d\bar{s} [\rho(\bar{r}') N^{(1)}(\bar{r}')/E(\bar{r}') - \rho(\bar{r}') N^{(1)}(\bar{r})/E(\bar{r})] \times G(\bar{r}, \bar{r}') + N_3(\bar{r}) + N_4(\bar{r}) + \dots \quad (\text{A.13})$$

where  $N_3(\bar{r})$  and successive terms are related to the immediately preceding term by:

$$N_K(\bar{r}) = k_0 \rho(r) \int d\bar{\Omega}/4\pi \int d\bar{s} N_{(k-1)}(\bar{r}') G(\bar{r}, \bar{r}') . \quad (\text{A.14})$$

The main attribute of Eq. (A.13) is that its leading term is close to the final solution and it was felt that numerical errors in the calculation of G would not propagate to the same extent as in Eq. (A.1).

Convergence requires roughly half as many terms as the medium is optically thick, if the series is terminated when the last term adds less than 0.1% of the sum of the preceding terms at all mesh points.

A spherical coordinate system was chosen with the origin at the cloud center and the polar ( $\theta=0$ ) axis along the sun-cloud line ( $\bar{\Omega}_g$ ), as shown in Figure 9. Since the solar flux is symmetric about the polar axis, the excited state distribution will also have cylindrical symmetry about that axis,  $N(\bar{r}) = N(r, \theta)$ . Therefore we need only find  $N(\bar{r})$  for  $0 \leq r < \infty$ ,  $0 \leq \theta \leq \pi$ . The radial mesh interval chosen was  $\Delta r = g/4$  where  $g$  is the folding distance of the spherically symmetric Gaussian ground state distribution

$$\rho(r) = \rho_0 \exp(-r^2/g^2) , \quad (\text{A.15})$$

and the cloud was terminated at  $n = 3g$ . The  $\theta$ -interval was chosen to be  $\pi/8$ , as was the  $\varphi$  interval. For numerical solution the value of  $N(r, \theta)$  was determined for each  $r$  and  $\theta$  mesh point. Equation (A.14) involves a three dimensional integration, but  $N_{(k-1)}(\bar{r}')$  is independent of  $\varphi'$ , while  $G(\bar{r}, \bar{r}')$  still is  $\varphi'$  dependent. So the  $\varphi'$  integration (carried around the torus indicated in Figure 9) may be incorporated into G and (A.14) rewritten

$$N_k^{IJ} = \sum_{I', J'} G_{I' J'}^{IJ} N_{(k-1)}^{I' J'} \quad , \quad (A.16)$$

with I and J representing the radial and angular variables. To obtain G each volume element was further divided into 8 subelements. But it was still necessary to find the self-contribution of each element  $G_{IJ}^{IJ}$ , not from direct integration, but by using Eq. (A.12) to write

$$G_{IJ}^{IJ} = 1 - E_I - \sum_{I', J' \neq I, J} G_{I' J'}^{IJ} \quad (A.17)$$

and, in a sense, normalizing the self-contribution to account for numerical mistakes in the other elements and to conserve photons.

An example of the excited atom distribution obtained is shown in Figure 10. Even though the full series solution  $N(\bar{r})$  differs from the first order approximation  $N^{(1)}/E$  along the sun-cloud line, they track almost perfectly through the center at right angles to that line. Since our observations were made nearly at right angles to the sun-cloud line we were able to save considerable computing time by using the  $N^{(1)}/E$  approximation to generate Figure 3. It was necessary to find the final solution to be sure that the approximation was valid.

For handling optical depth effects on the  $\lambda 4934$  ion line we desired only to find a first approximation, since the cross excitation between ground and metastable levels is much more important than in the neutral case, and since the real geometry is completely intractable. The approximation we have chosen is to assume that radiation transport will supply an excited ion distribution proportional to the ground state

distribution, and the only optical depth effects come from reabsorption of emitted radiation before it reaches the detector. One justification for this approximation is that in applying this crude model to the neutral cloud it supplied a half-width that agreed with the full transport solution to within 15% over a range of optical depths from 0.01 to 1000. An increase in the optical depth of the medium is manifested by a decrease in the ratio of the main to hyperfine component from its optically thin value of 14.7 (see Figure 7). We have attempted to relate this ratio to the optical depth (ion line of sight density).

To implement this approximation Eq. (A.10) is rewritten in terms of optical depth instead of distance,  $d\tau = k_0 \rho(r) ds$ ;

$$I(x, \bar{N}_0) = \text{const} \cdot \int_0^{\tau} \alpha(x) \exp[-\alpha(x)\tau'] N(\tau') d\tau' \quad (\text{A.18})$$

where  $N(\tau') = N(\bar{r}') / (k_0 \rho(r'))$ . At line center  $x = 0$  and using  $N(\tau') = \text{constant}$  ( $N(\tau) \propto \rho(\tau)$ )

$$I_0 = \text{const} \times N(\tau) [1 - \exp(-\tau)] \quad (\text{A.19})$$

Now, since both main (m) and hyperfine (hf) level populations are assumed proportional to the ground state population,  $N_m(\tau) = 14.7 N_{hf}(\tau)$  and  $\tau_m = 14.7 \tau_{hf}$  we may take the ratio of main to hyperfine peaks:

$$I_{cm}/I_{ohf} = [1 - \exp(-\tau)] / [14.7(1 - \exp(-\tau/14.7))] \quad (\text{A.20})$$

where now  $\tau$  refers to the optical depth of ions responsible for absorbing



the main component, i.e. 82% of the total in the ground state. The predicted main to hyperfine ratio (Eq. (A.20)) has been plotted in Figure 11 against  $T$  which is defined as the optical depth of all ions in the ground state, i.e.  $T = \tau/.82$ . Figure 11 has then been used for our reduction of the ion line data.

In the late stages of this research an investigation was made into using emission and absorption profiles which are more general than the Gaussian profiles initially used in the neutral barium line shape calculations. It was not feasible to include natural line broadening in the transport section of the calculations (determining the spatial distribution of atoms in the upper level), although it is planned to do this in the future. However, the appropriate Voigt (natural plus doppler broadening) profile has been used for the emission and absorption profiles which enter the line-of-sight integration for the recorded profile. That is,  $\alpha(x)$  in Eq. (A.10) has been replaced by the Voigt function  $v(x)$ , where

$$v(x) = \frac{a}{\pi} \int_{-\infty}^{\infty} \frac{e^{-y^2}}{a^2 + (x-y)^2} dy \quad , \quad (A.21)$$

and "a" is the ratio of natural to doppler line widths. Figs. 3, 4 and 5 have been produced using the results of these hybrid calculations.

## References

1. G. Haerndel and R. Lust, "Artificial Plasma Clouds in Space", Scientific American, November 1968, p. 81.
2. L. Haser, "Use of Artificial Barium Clouds to Study Magnetic and Electric Fields in the Atmosphere", in Aurora and Airglow, Ed. B. M. McCormac, Reinhold Publ. Co., New York, Amsterdam and London, 1967, p. 391.
3. H. Foppl, G. Haerndel, L. Haser, J. Loidl, P. Lutjenz, R. Lust, F. Melzner, B. Meyer, H. Neuss, and E. Rieger, Planet. Space Sci. 15, 357 (1967).
4. N. W. Rosenberg, G. T. Best, F. P. Delgreco, M. M. Klein, M. A. MacLeod, T. M. Noel, and W. K. Vickery, "AFRL Barium Release Studies 1967", Ed., R. S. Leonard. Stanford Research Institute Special Report No. 4, Stanford, California (1969).
5. G. E. Thomas, J. Geophys. Res. 68, 2639 (1965).
6. N. W. Rosenberg, "Barium Releases, Puerto Rico, May 1968", Air Force Cambridge Res. Lab., Bedford, Massachusetts (unpublished).
7. U. S. Standard Atmosphere Supplement, 1966, U. S. Government Printing Office, Washington, D. C. (1966).
8. Preliminary Results of Test Series SECEDE III, Ed., R. S. Leonard, Stanford Research Institute Report RADG-TR-69-239, Vol. I, Stanford, California (1969).
9. O. Harang and W. Stoffregen, Planet. Space Sci. 17, 261 (1969).
10. K. H. Lloyd, Planet. Space Sci. 17, 1683 (1969).
11. B. Kivel and M. B. Saxe, "Structure of Spectral Lines of BaI and BaII", Research Note 811; and E. R. Bressel and B. Kivel, "Voigt Profiles for the Barium Ion Resonance Line at  $4934\overset{\circ}{\text{A}}$ ", Research Note 808, Avco Everett Res. Lab., Everett, Mass. (1969).

12. G. N. Oetzel and N. J. F. Chang, "Analysis of SECEDE III HF Data", Stanford Research Institute Report RADC-TR-69-412, Stanford California (1969).
13. R. W. Deuel and R. D. Sears, "Interferometric Measurements on SECEDE I Barium Releases", IIT Research Institute Report RADC-TR-68-465, Chicago, Illinois (1968).
14. T. N. Davis, private communication, and Ref. 7, p. 94.
15. M. V. Biondi, R. Hake, and D. Sipler, "Preliminary Optical Interferometer Results", Preliminary Results of Test Series Secede III, Ed. R. S. Leonard, Stanford Research Institute Report RADC-TR-69-239, Vol. I, Stanford, California (May 1969).
16. The 100 mm aperture Fabry-Perot plates were fabricated by the Perkin-Elmer Corporation to  $\lambda/100$  flatness and coated with broad-band (4900-6350A) dielectric coatings of high reflectivity.

## Figure Captions

- (1) Sample of real time chart records obtained during barium releases. These scans show  $\lambda 4934$  and  $\lambda 5535$  lines from the early moments of event Gum. The information in the indicated channels is as follows:
- Channel information
- 1, 6 Interference filter code (not operational here)
  - 2 Gamma-scope memory, showing buildup of lines
  - 3, 8 10<sup>th</sup> channel marker
  - 4 Pressure transducer with filter change and start signals superimposed
  - 5, 10 Serial time code (GMT, erratic operation here)
  - 7 Monitor scalar (photometer)
  - 9 FP scaler (single pass line profiles)
- (2) Partial term diagrams for neutral and ionized barium, with the transitions we have studied listed by wavelength in Å. Also shown are the metastable levels and some levels which link the metastables together and to the ground level.
- (3) Observed  $\lambda 5535$  contrast finesse for barium release GUM, and curves showing predicted variation of contrast finesse for a cloud of constant inventory evolving by diffusion, labelled by the total Ba in the cloud.
- (4) Experimental  $\lambda 5535$  profile at  $R + 45$  seconds for event GUM, and predicted profiles for different combinations of barium temperature and inventory. Only half of the (symmetric) profiles are shown and the experimental profile has been folded about its midpoint to enhance the comparison.

- (5) Time variation of  $\lambda 5535$  in event GUM. Vertical axis is relative intensity. Model curves have been normalized to experimental curves at  $R + 2$  min.
- (6) Time variation of  $\lambda 5826$  in event GUM. Vertical axis is relative intensity. Smooth curves are visual fits to data points. Time is GMT(Z).
- (7)  $\lambda 4934$  profile observed at  $R + 26$  minutes in event GUM, and calculated profile for no absorption. The arrows indicate centers of gravity of closely grouped lines and their relative intensities. The peak at  $\sim 75$  on the frequency scale is the "hyperfine line".
- (8) Time variation of  $\lambda 4934$  in event GUM. Vertical axis is relative intensity, time is GMT(Z). Subsidiary component is the "hyperfine" line.
- (9) Resonance radiation transport geometry. Since the exciting solar flux (incident along  $\bar{\Omega}_s$ ) is symmetric about the z-axis, as is the ground state Ba density, then the excited state density will be also. Therefore, a solution need only be found in a semicircular plane, shown hatched in the plane of the figure. The three-dimensional path which must be employed to find the transfer matrix  $G(\bar{r}, \bar{r}')$  is indicated by an ellipse. The line of sight (along  $\bar{\Omega}_o$ ) integration for the line profile is carried from one edge of the cloud to the other, through the origin and perpendicular to the z-axis ( $\bar{\Omega}_o \perp \bar{\Omega}_s$ ).
- (10) Excited state densities along  $\bar{\Omega}_s(||)$ . and along  $\bar{\Omega}_o(\perp)$  (see Figure 9).  $N^{(1)}$  is the density excited by primary solar flux (absorbed but not scattered),  $N^{(1)}/E$  is the Sobolev (see text) approximation to the final solution, and  $N$  is the final solution.

- (11) First approximation to optical depth effects on  $\lambda 4934$ . The curve gives the value of line of sight ion ground state density which would produce a given main/hyperfine ratio in  $\lambda 4934$ , under the uniform excitation approximation ( $N(\bar{r}) \propto \rho(\bar{r})$ ).
- (12) Solid points:  $\lambda 4934 \text{ \AA}$  line profiles obtained during event Spruce (R = 23:52:04Z). Solid curve: computer-generated optically thin profiles adjusted to fit the  $\lambda 4934$  hf line in height and half-width. The unabsorbed peak intensity is 100 units.
- (13) Successive spatial scans in hf light over a portion of the Spruce ion cloud showing a fine-scale striation. Scans from left to right.
- (1) 00:11:59 to 12:65Z, (2) 12:13 to 12:19, (3) 12:32 to 12:38,  
(4) 12:49 to 12:55.
- (14) Spatial scan in hf light and in total  $\lambda 4934$  light of Spruce leading edge showing shape differences due to optical depth effects. Scans from left to right from 00:19:37 to 19:50Z.
- (15) Three spatial scans nearest in time to beacon occultation on event Spruce. Scan was performed from left to right.

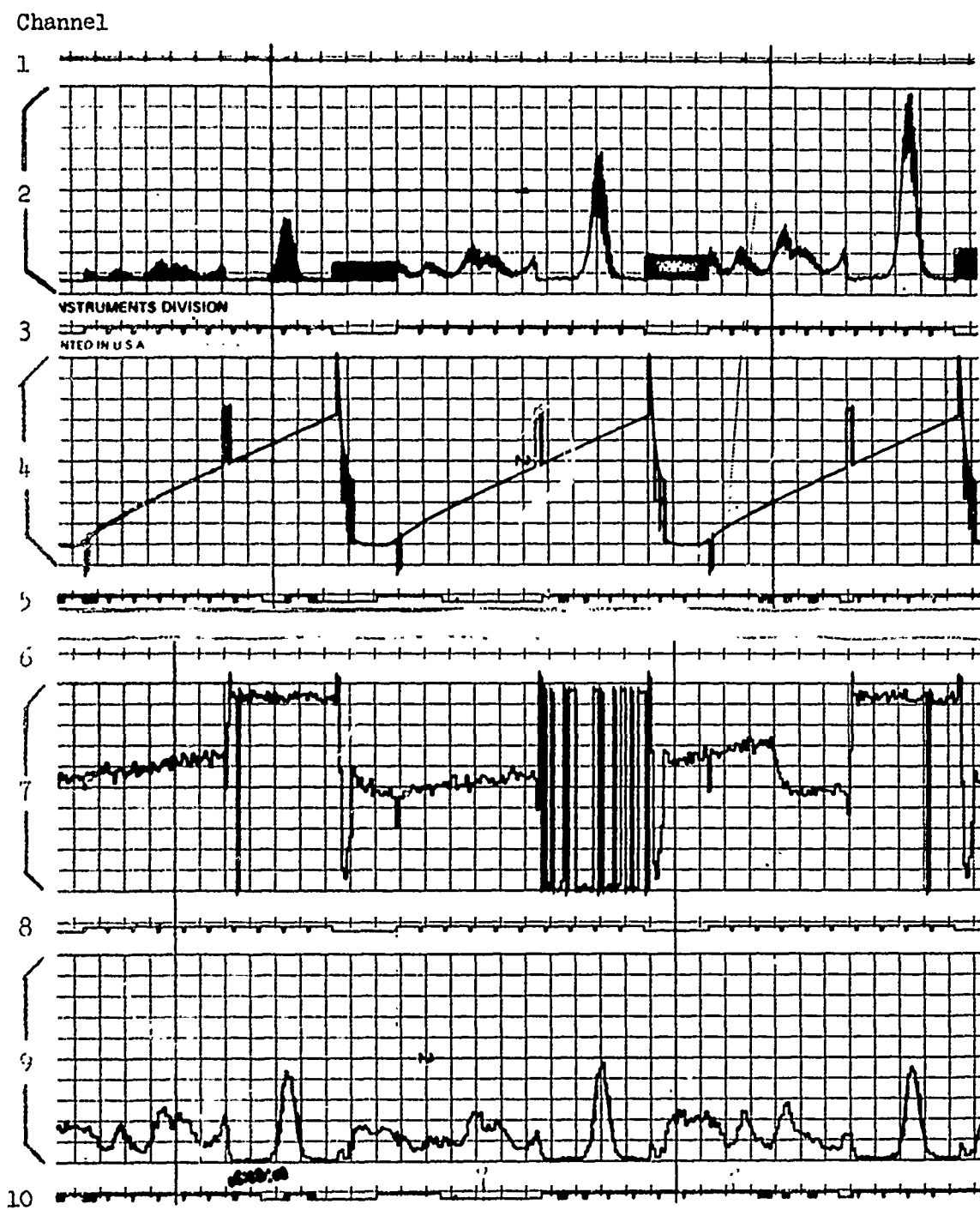


Figure 1.



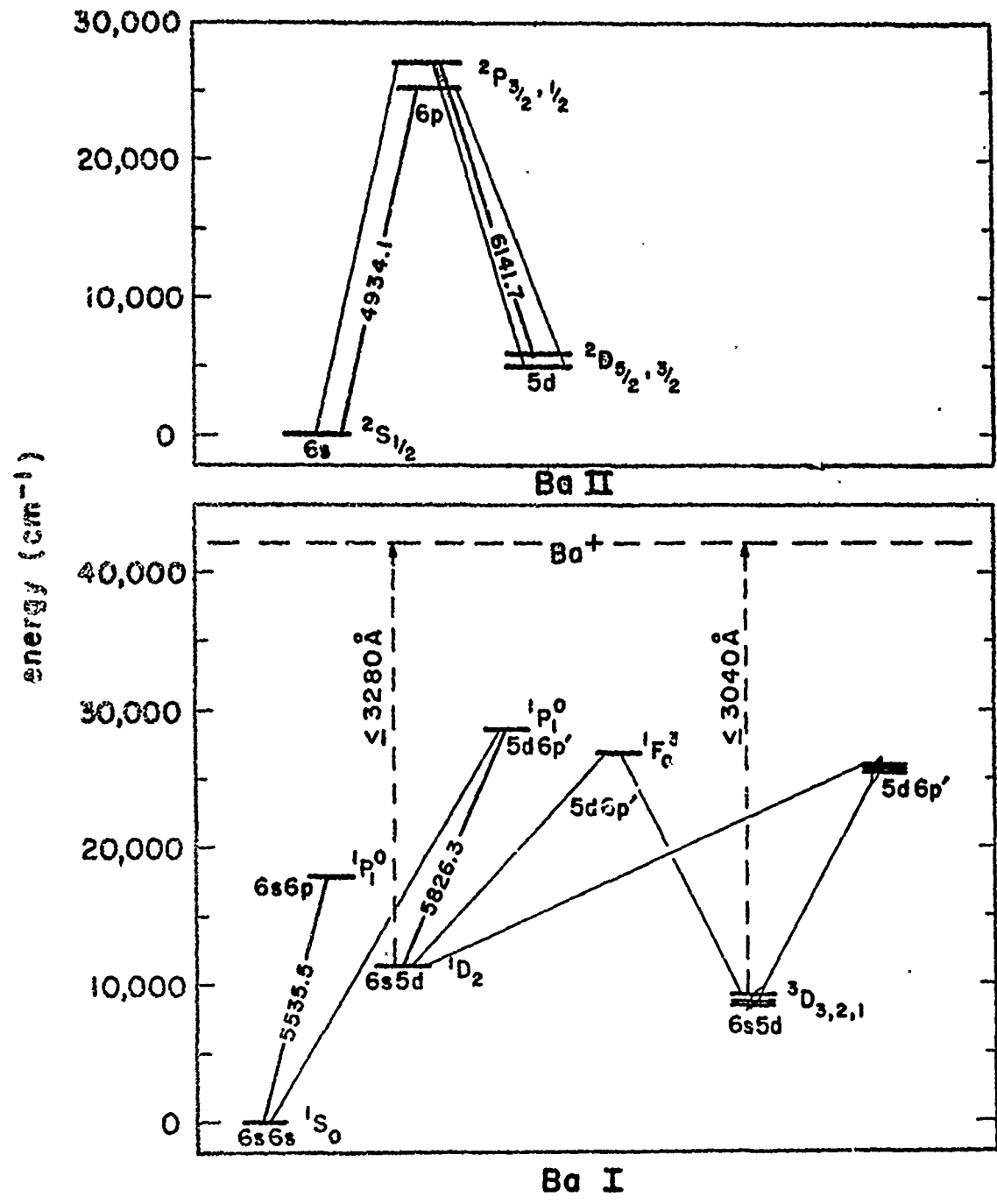
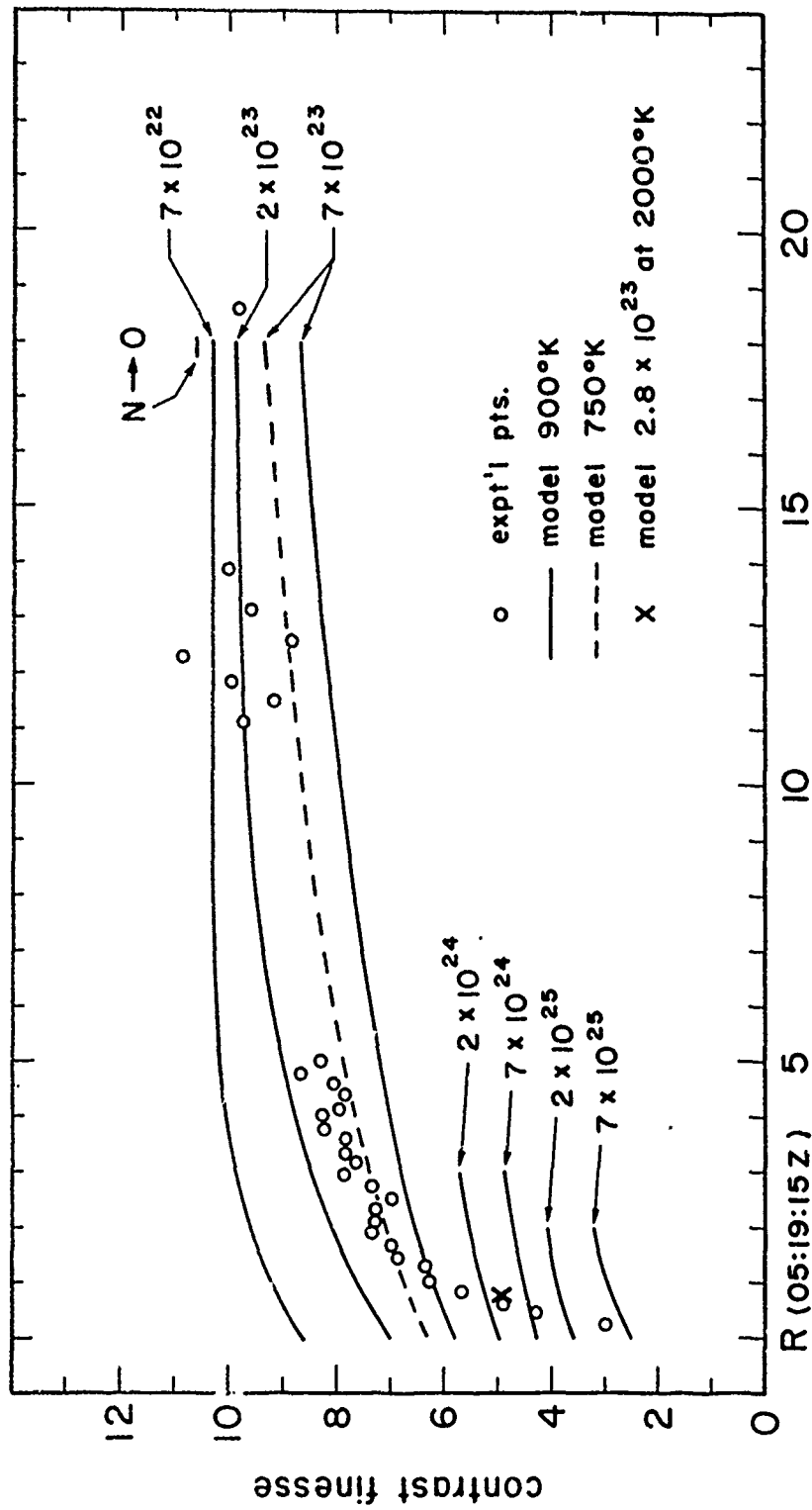


Figure 2.





time after release (minutes)

Figure 3.

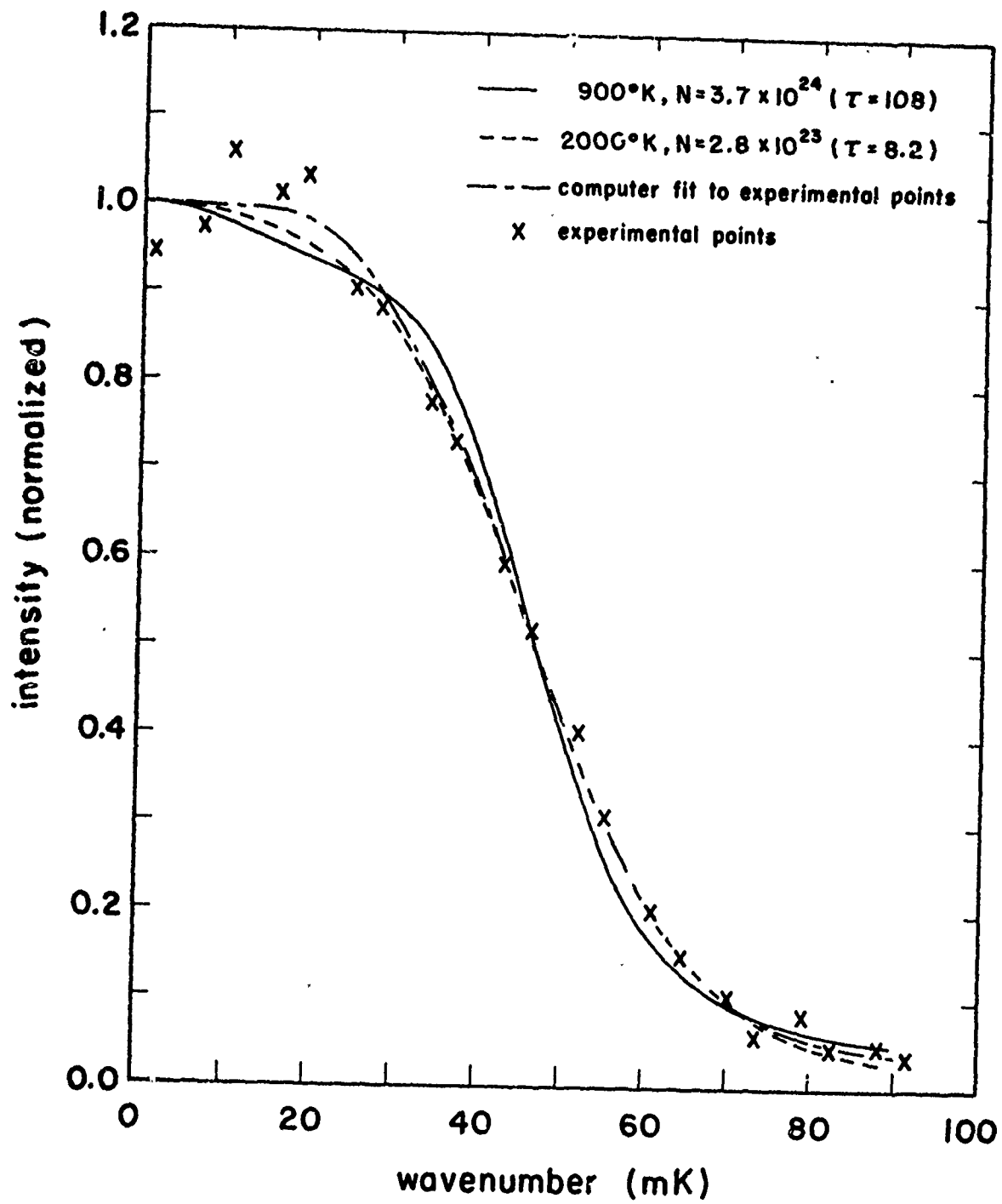


Figure 4.

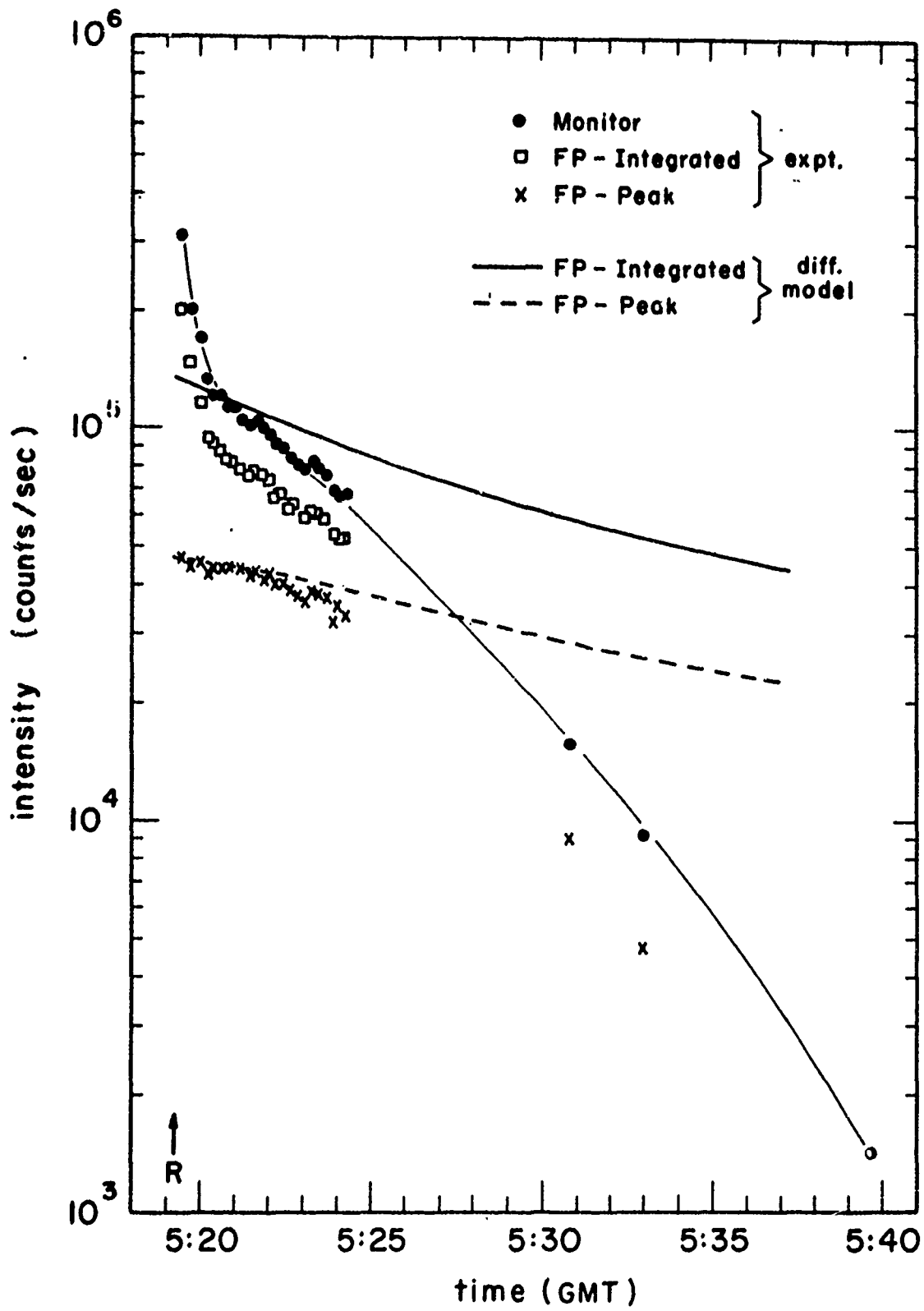


Figure 5

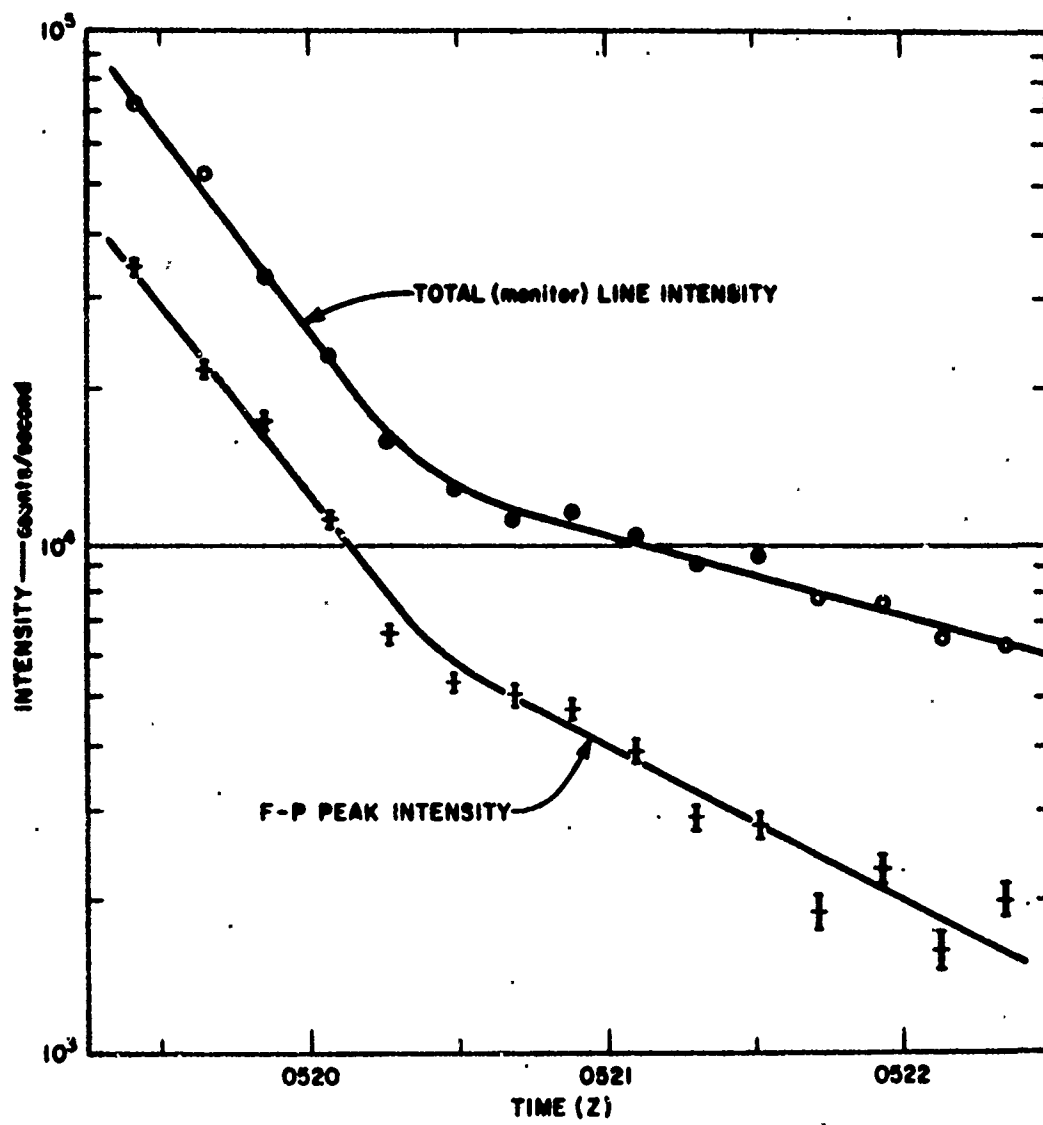


Figure 6.

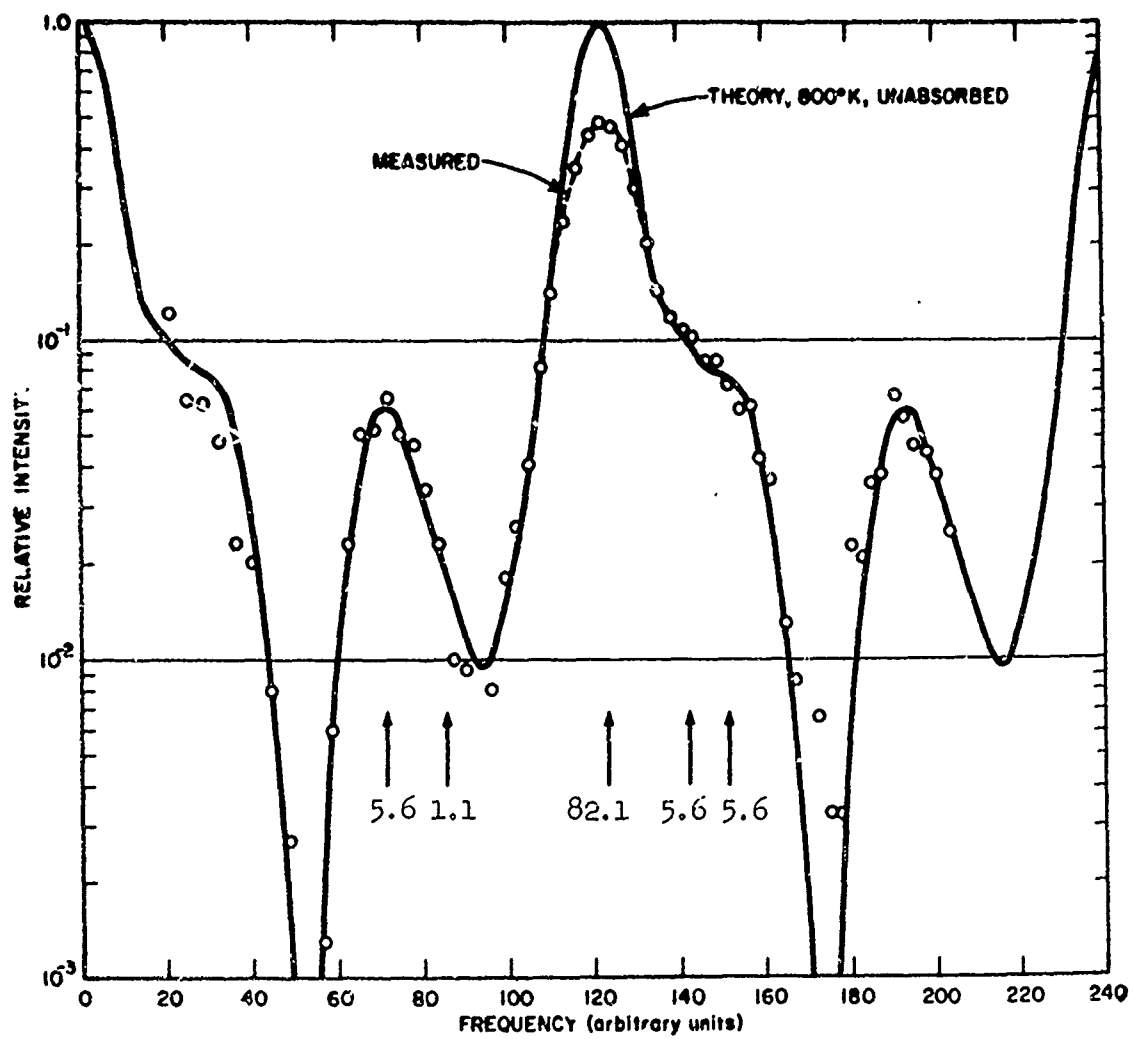


Figure 7.

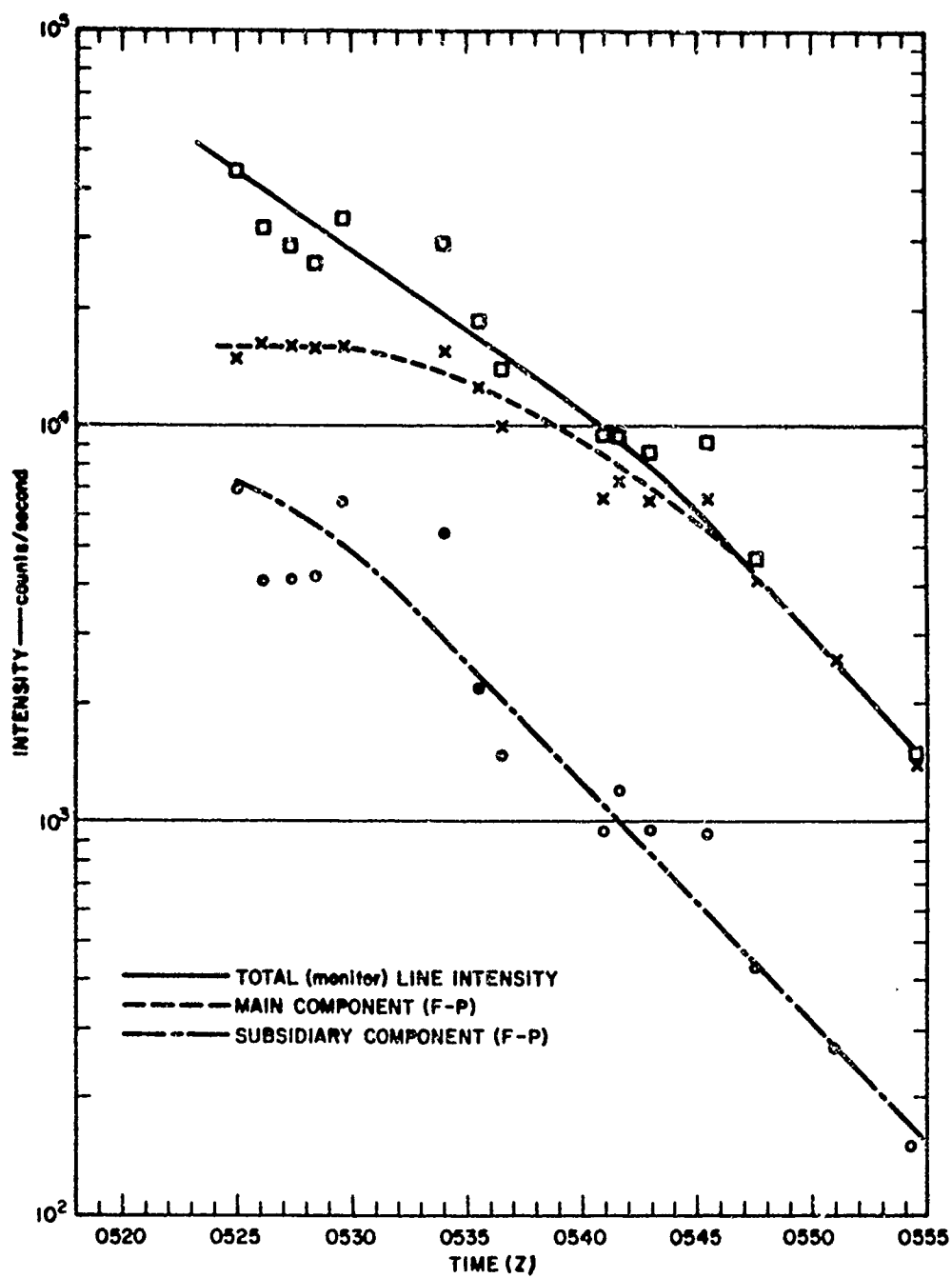


Figure 8.

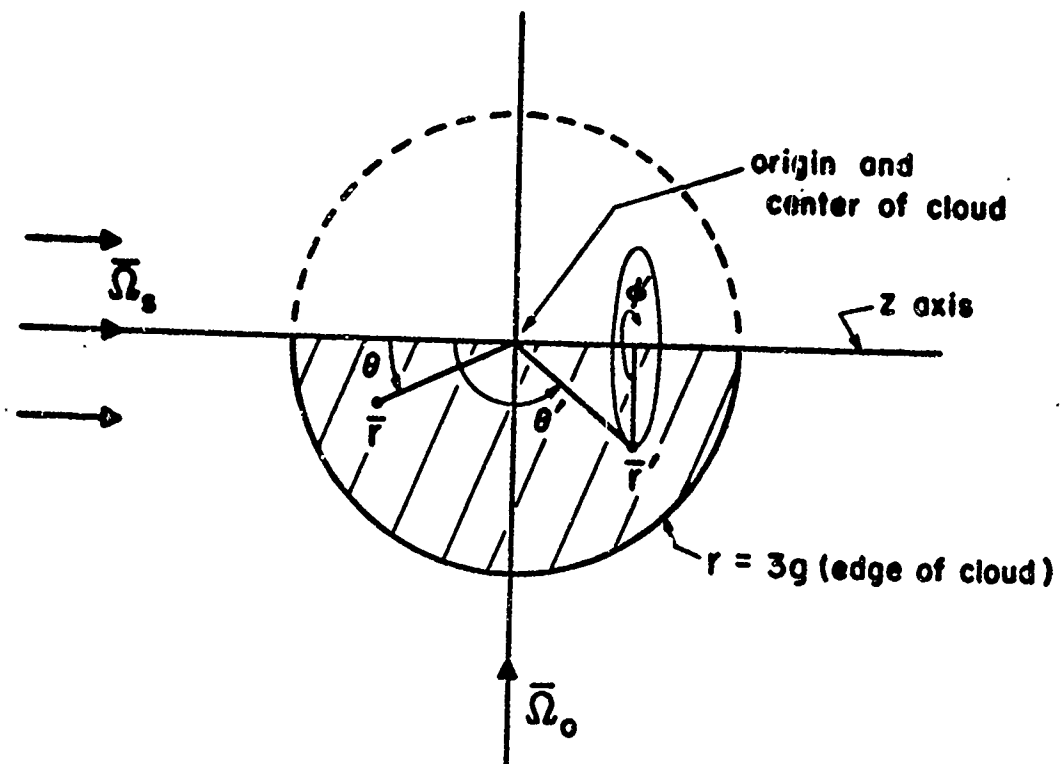


Figure 9.

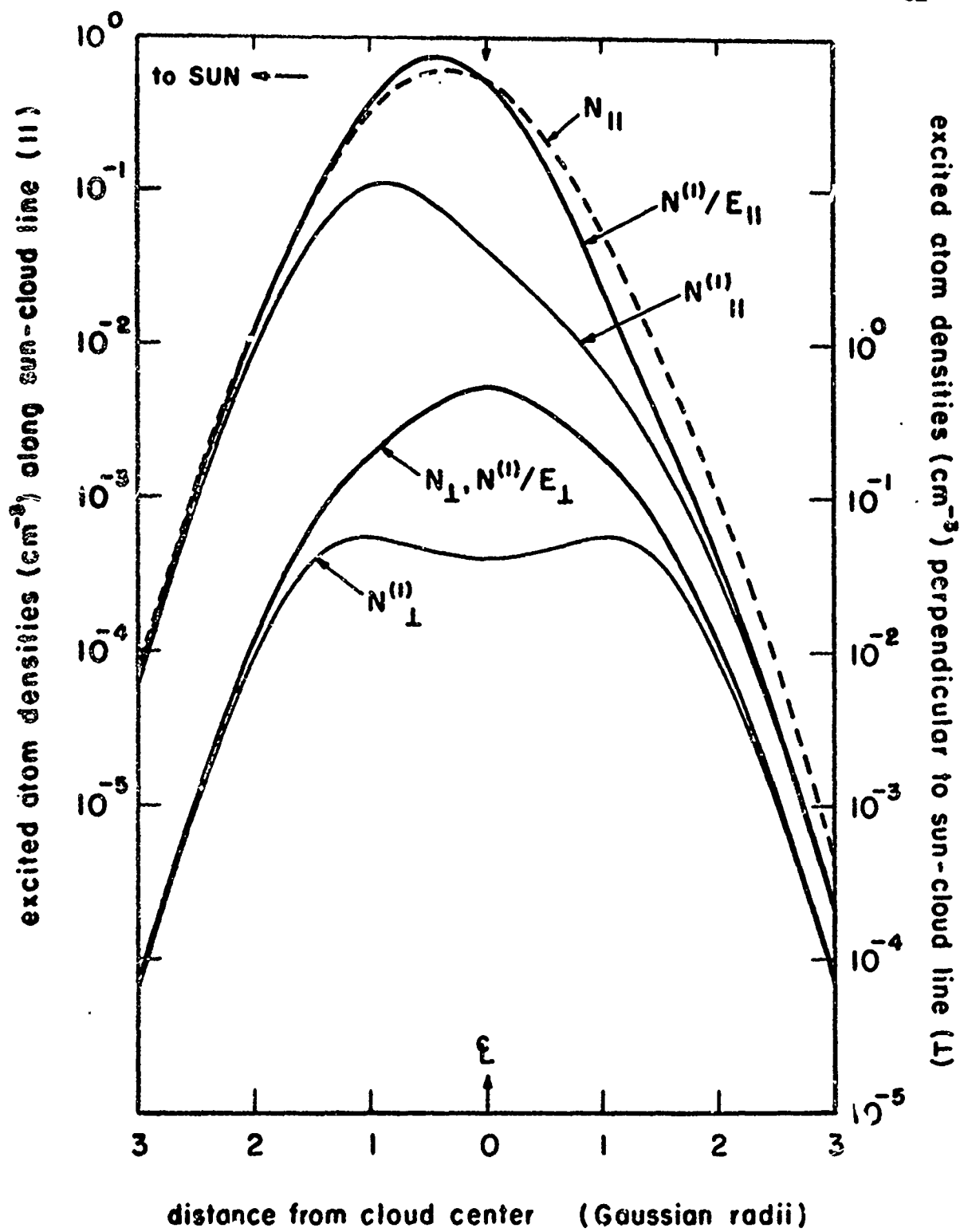


Figure 10.



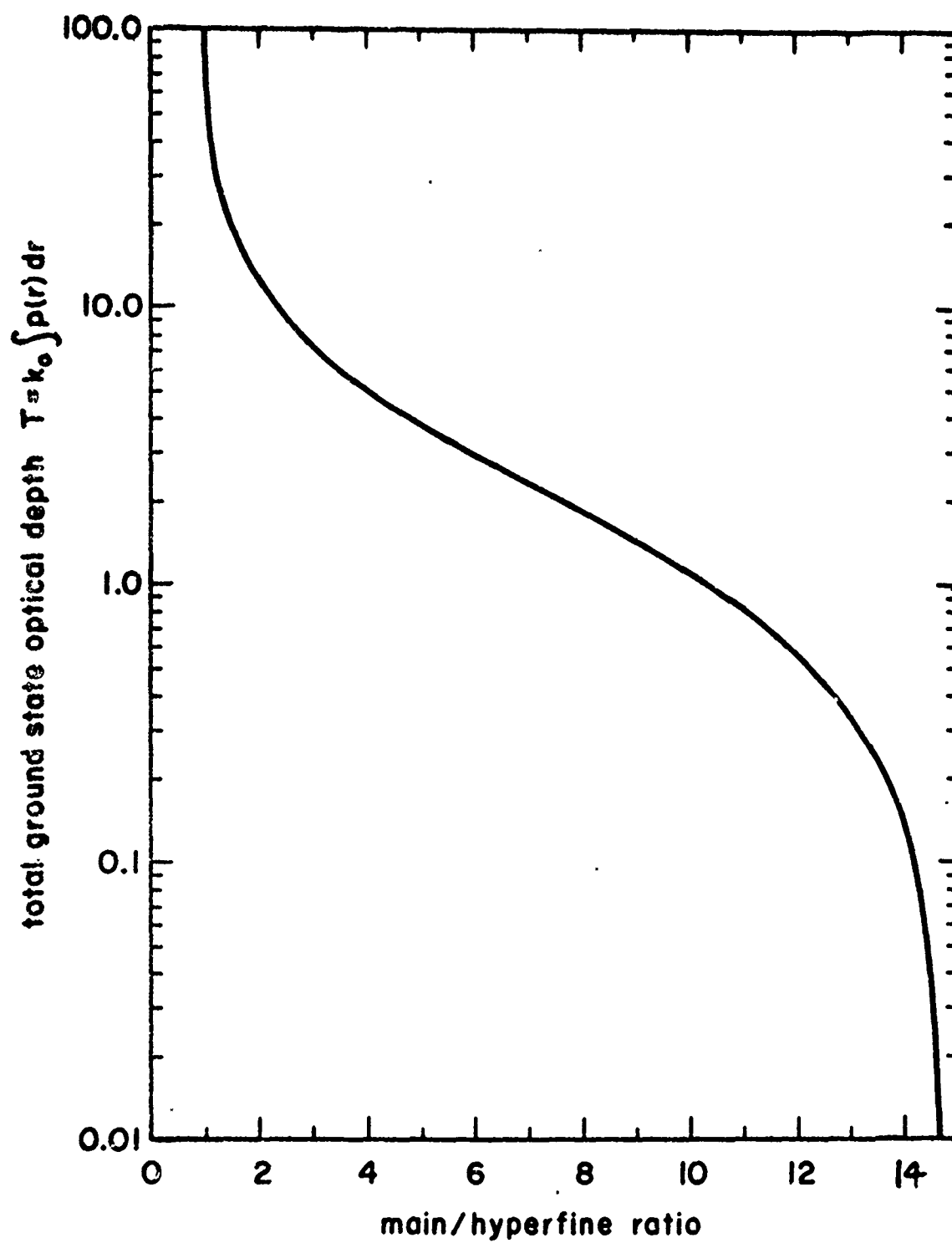


Figure 11

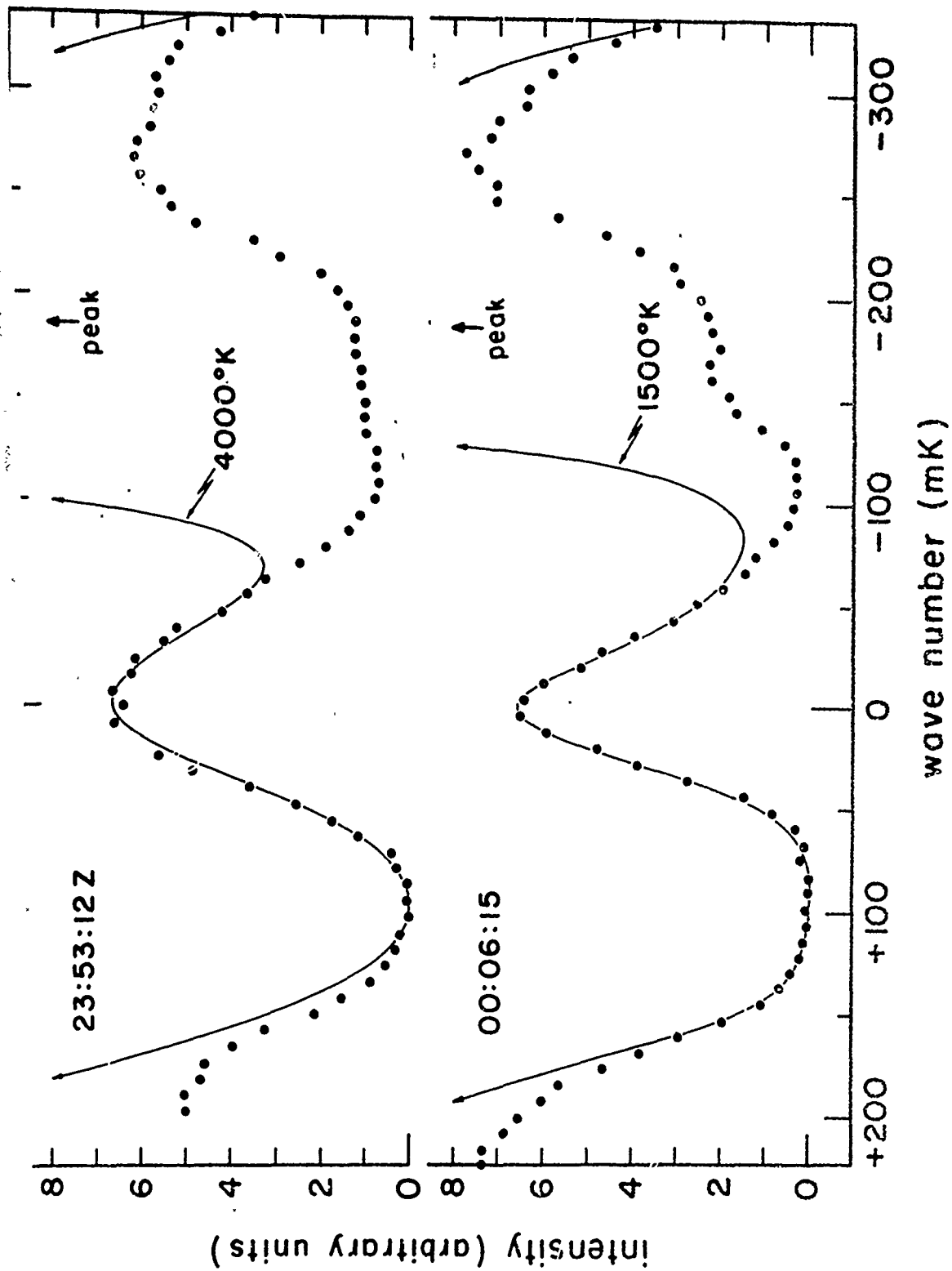


Figure 12

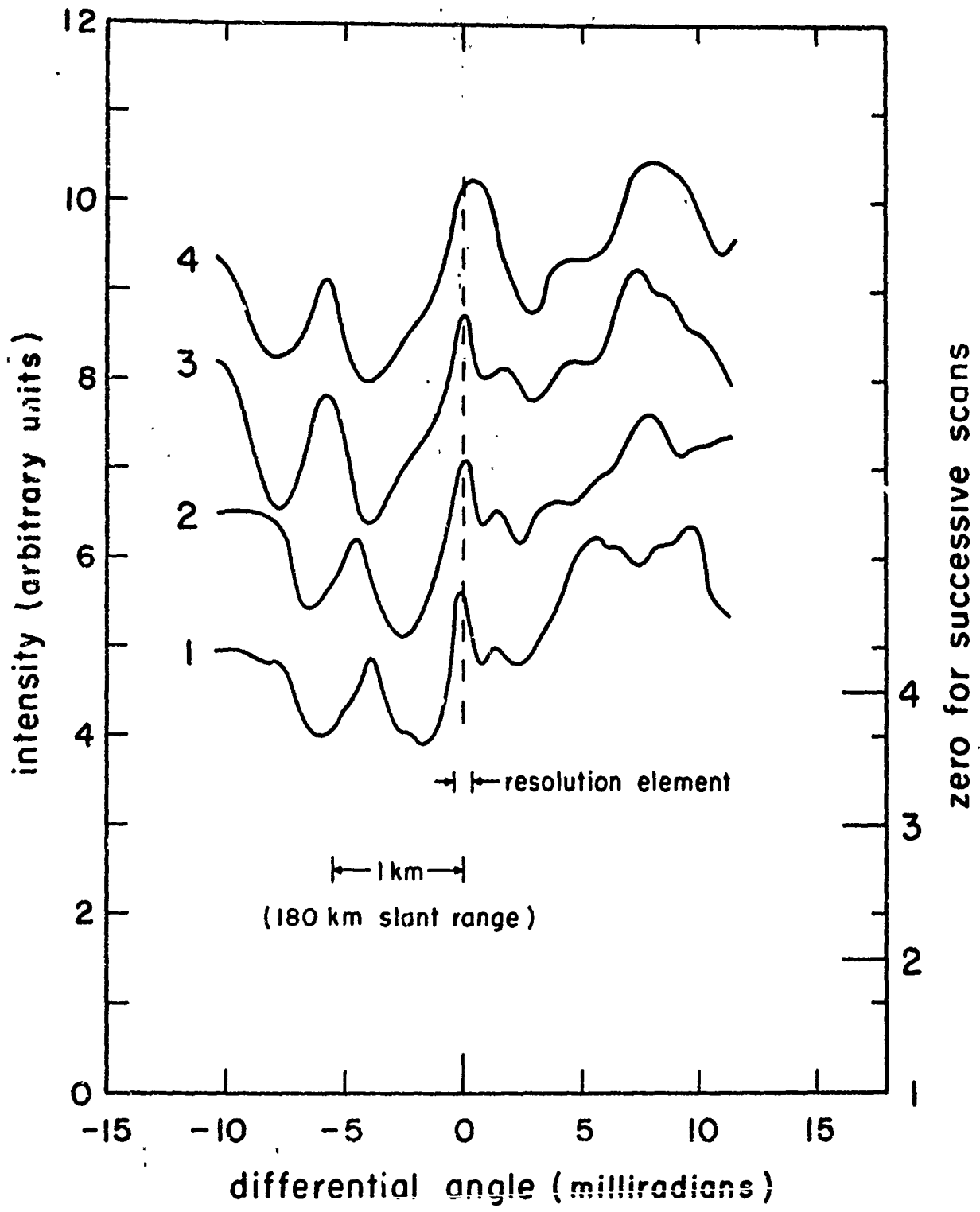


Figure 13

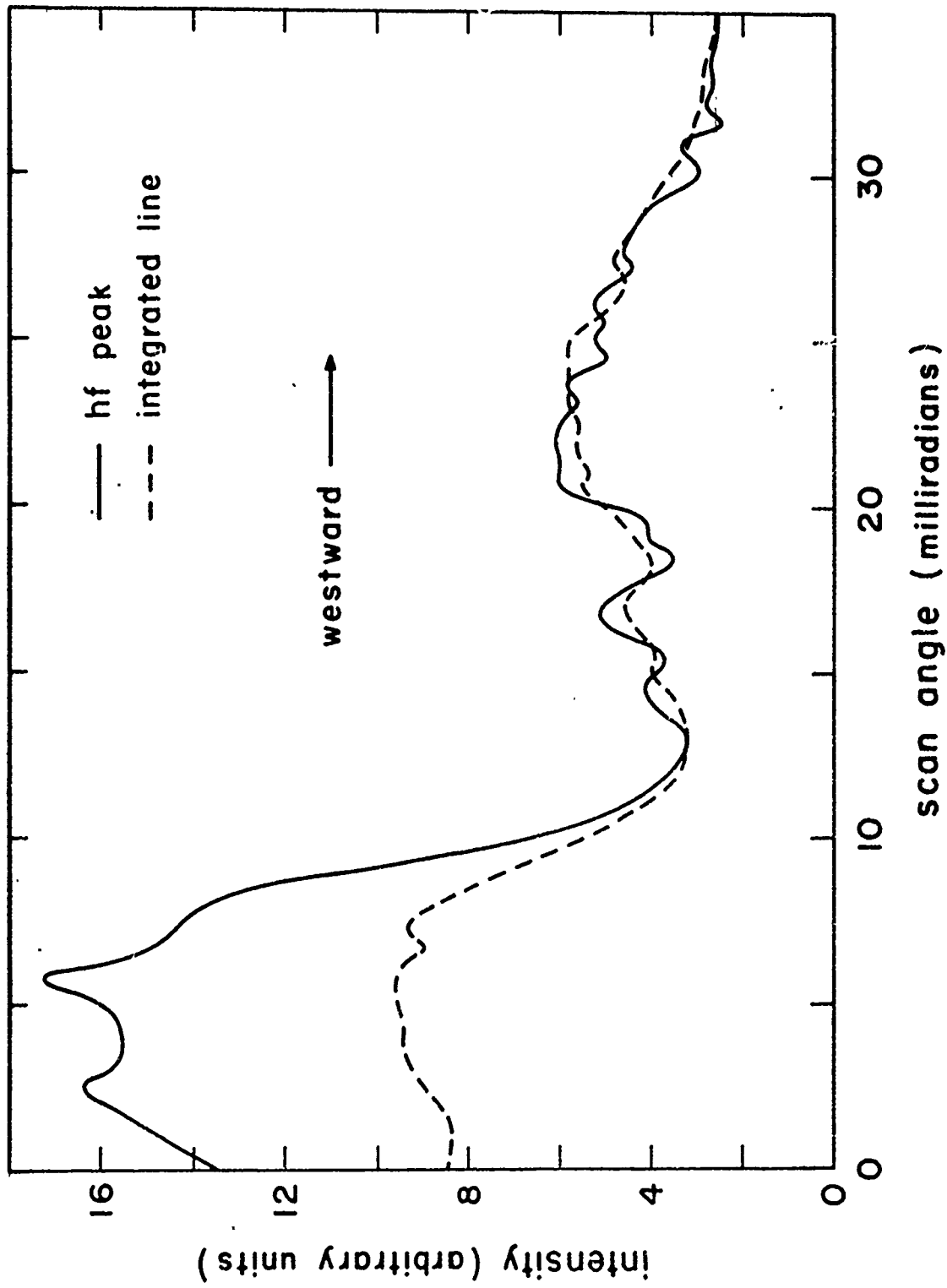


Figure 14

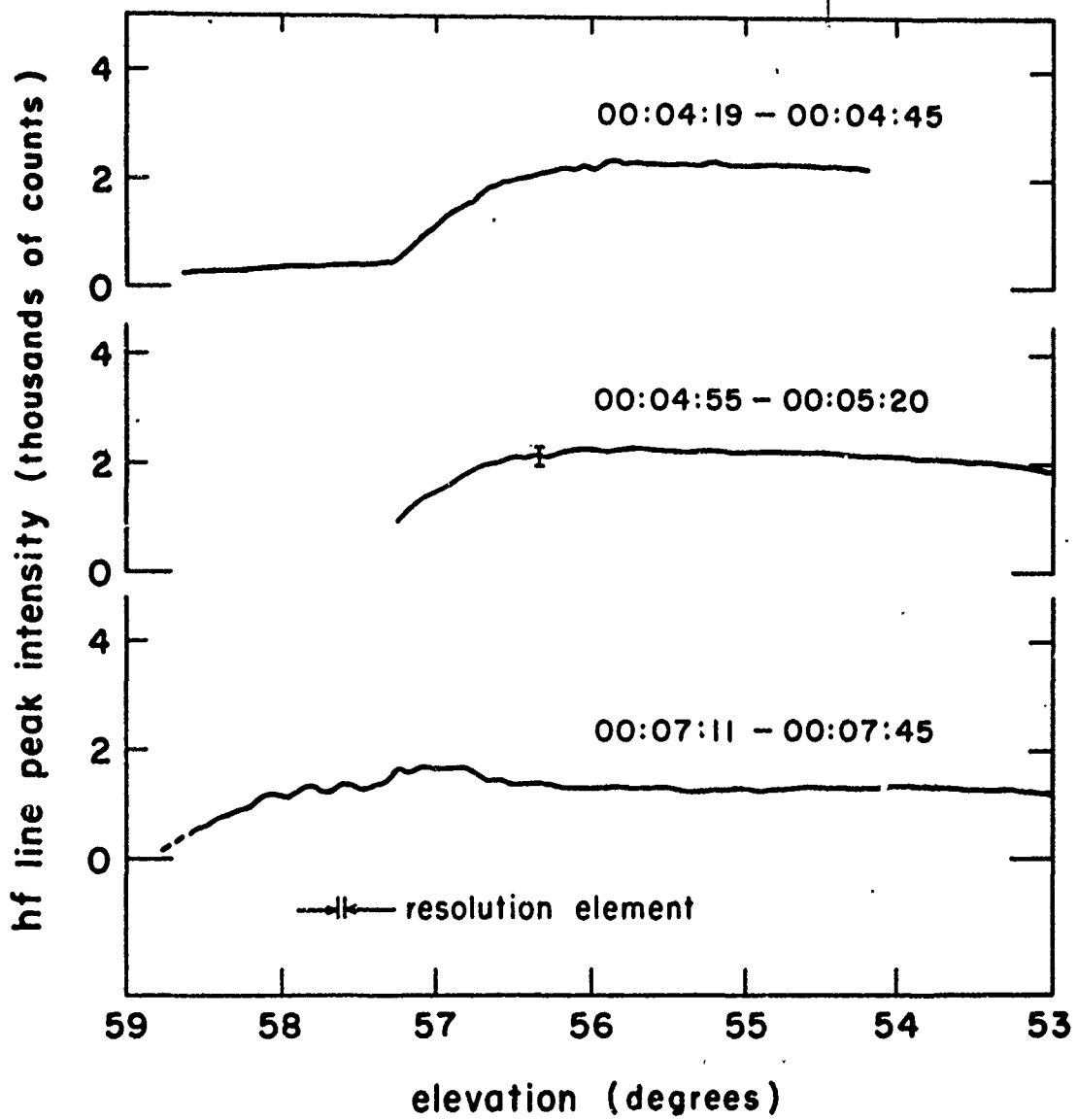


Figure 15